Distinct contributions and sensorimotor encoding of PV and FoxP2 neurons in the external globus pallidus during perceptual decision-making

Xiaotian Pu[1,2], Jingyu Ren[1,2], Taorong Xie[1], Kexin Zou[1,2], Jingze Xu[1,2], Yaping Li[1], Dechen Liu[1,*], and Haishan Yao[1,3,*]

[1]Institute of Neuroscience, State Key Laboratory of Brain Cognition and Brain-inspired Intelligence Technology, CAS Center for Excellence in Brain Science and Intelligence Technology, Chinese Academy of Sciences, Shanghai 200031, China

[2]University of Chinese Academy of Sciences, Beijing 100049, China

[3]Lead Contact

[*]Correspondence: dcliu@ion.ac.cn (D.L.), haishanyao@ion.ac.cn (H.Y.)

SUMMARY

The external globus pallidus (GPe), a central nucleus of the basal ganglia (BG), comprises diverse cell types, including PV and FoxP2 neurons. While previous studies have delineated their distinct roles in movement regulation and sensory processing, their contributions to perceptual decision-making remain unclear. Here we investigated the sensorimotor functions of PV and FoxP2 neurons in mice performing a Go/No-Go visual task. Optogenetic activation of either population impaired task performance, whereas only inhibition of PV — but not FoxP2 neurons—disrupted behavior. Electrophysiological recordings revealed that PV and FoxP2 neurons exhibited distinct encoding of visual stimuli, licking movement, and trial outcomes. Moreover, inhibiting GPe PV neurons altered stimulus and outcome selectivity, as well as task-related activity, in the substantia nigra pars reticulata, a major output nucleus of the BG. These findings reveal that GPe PV and FoxP2 neurons uniquely regulate the flow of sensorimotor information within the BG during perceptual decision-making.

KEYWORDS

External globus pallidus, Parvalbumin neurons, FoxP2 neurons, Sensorimotor processing, Electrophysiology, Substantia nigra pars reticulata

INTRODUCTION

The external globus pallidus (GPe), a central nucleus in the basal ganglia (BG), plays a crucial role in motor control and cognitive functions.[1-7] Traditionally, the GPe was viewed primarily as a relay nucleus in the indirect pathway of the BG circuit, where its GABAergic neurons receive inhibitory inputs from striatal medium spiny neurons expressing the D2-type dopamine receptors (D2-MSNs) and excitatory inputs from the subthalamic nucleus (STN), and project to STN and the BG output nuclei, the substantia nigra pars reticulata (SNr) and internal globus pallidus (GPi).[8,9] Emerging evidence, however, has revealed that the GPe is more than a simple relay; it forms extensive connections with all major BG components, as well as with the thalamus and cortex.[3-5,10,11] Moreover, the GPe consists of diverse cell types that differ in their projection patterns, molecular profiles, electrophysiological characteristics, and functional properties.[4,5,11,12]

Early research identified a dichotomous organization within the GPe: prototypic neurons are tonically active and innervate canonical downstream nuclei such as the STN, and arkypallidal neurons are characterized by lower spike rates and project back to the striatum.[13-15] Molecularly, GPe neurons are divided into distinct populations, with approximately 50% expressing parvalbumin (PV) and around 20% expressing forkhead box protein P2 (FoxP2).[15-18] GPe PV neurons display prototypic properties, innervating the STN, SNr, and parafascicular nucleus (PF) of the thalamus.[10,16] These neurons also contain subpopulations that co-express other molecular markers.[19] In contrast, GPe FoxP2 neurons exhibit arkypallidal properties, exclusively innervating the striatum.[14]

The FoxP2 neurons are a major subclass of neurons expressing neuronal PAS-domain-protein-1 (Npas1), which make up about 30% of GPe population and do not overlap with PV-expressing neurons.[15,16,19,20] This cellular diversity necessitates a cell-type-specific approach to investigating GPe function.

Behavioral significance of specific GPe cell types has been explored in various studies. In vivo recordings have shown distinct activity patterns of prototypic and arkypallidal GPe neurons during movements.[15,21] In healthy mice, optogenetic activation of PV-expressing GPe neurons enhances locomotor activity, whereas their inhibition suppresses it.[18,20,22] Conversely, activation of GPe Npas1 or FoxP2 neurons reduces locomotor speed,[18,20,23-25] while Npas1 neuron inhibition increases locomotion.[20] Combinatorial movement metrics reveal that optogenetic stimulation of GPe FoxP2 neurons induces behavioral changes similar to those of Npas1 activation but opposite to those elicited by PV stimulation.[18] Recent studies further highlight the contribution of specific GPe cell types in regulating movement, hypokinetic symptoms, or dyskinetic behaviors in mouse models of Parkinson's disease (PD).[20,22,26-29] Beyond motor control, GPe neurons have also been implicated in non-motor functions.[1,3,6,30] For example, they encode information related to value, salience, and valence.[31-34] GPe arkypallidal neurons participate in movement suppression in a stop-signal task[21] and regulate habitual seeking behaviors,[35] while GPe PV neurons mediate behavioral punishment[36] and control cocaine sensitivity,[37,38] highlighting their important contribution to decision-making processes and related cognitive functions. In anesthetized mice, prototypic and arkypallidal GPe neurons exhibit distinct response

patterns to tactile sensory stimulation,[39] which are attributed to their different input sources from the striatum and STN.[40] Collectively, these studies underscore the integrative role of the GPe in processing diverse motor and non-motor signals. However, it remains unclear how different types of GPe neurons contribute to sensorimotor function and encode task-related signals during perceptual decision-making, a process in which animals use sensory cues to guide appropriate motor responses. Furthermore, studies in PD mouse models have found that manipulating specific cell types in GPe alters SNr activity patterns and rescues motor behavior.[26,27] These findings raise the question of whether, and how, defined GPe cell types modulate sensorimotor signaling in the SNr under normal conditions.

In this study, we investigated the functional roles of PV and FoxP2 GPe neurons during a Go/No-Go visual task in mice. We found that selective activation of PV or FoxP2 neurons impaired task performance, whereas only inhibition of PV neurons caused behavioral deficit. Electrophysiological recordings showed that these two cell types differed in their encoding of stimulus, outcomes, and licking-related signals. Additionally, endogenous activity of GPe PV neurons modulated task-related responses in BG output neurons within SNr. These findings reveal distinct contributions of GPe neuron subtypes to sensorimotor processing during perceptual decision-making—an essential process for understanding how basal ganglia dysfunction contributes to disorders of motor and cognitive control.

RESULTS

Activation of either PV or FoxP2 neurons impairs Go/No-Go task performance

Head-fixed mice were trained to perform a Go/No-Go visual discrimination task[41] (Figure 1A), in which the Go and No-Go stimuli were vertical and horizontal gratings, respectively. The duration of stimulus presentation consisted of a waiting period and an answer period. During the answer period, licking in response to the Go stimulus was rewarded with water (Hit), while licking to the No-Go stimulus was false alarm (FA) and was not rewarded.

To examine the effect of activating PV or FoxP2 GPe neurons, we used PV-Cre or FoxP2-Cre mice (Figures 1B and 1C), in which AAV-FLEX-ChrimsonR was unilaterally injected into the GPe. In vivo recordings verified that optogenetic activation of ChrimsonR could increase the firing rates of GPe neurons (Figure 3). We trained the mice to perform the task by presenting visual stimuli contralateral to the virus injection site. After training, we applied red laser stimulation (635 nm, 0 – 3 s relative to stimulus onset) to the GPe during trials in laser-on blocks, which were interleaved with laser-off blocks (Figures 1B and 1C). We found that activation of GPe PV neuron significantly increased the FA rate ($p = 0.031$, $n = 6$, Wilcoxon signed-rank test, Figure 1E, top panel) as well as the Hit rate ($p = 0.031$, $n = 6$, Wilcoxon signed rank test, Figure 1D, top panel), with a significant decrease in discriminability (d') ($p = 0.031$, $n = 6$, Wilcoxon signed-rank test, Figure 1F, top panel). In control PV-Cre mice in which AAV-FLEX-EGFP were injected in the GPe, laser stimulation did not affect behavioral performance ($p > 0.5$, $n = 5$, Wilcoxon signed-rank test, Figures 1D–1F, top panels). Compared to the GFP mice, the ChrimsonR mice showed a significantly larger increase in FA rate

and greater reduction in d′ following laser stimulation ($p < 0.01$, Wilcoxon rank-sum test, Figures 1E and 1F, bottom panels). Similar to PV neuron activation, activating FoxP2 neurons in GPe also increased the FA rate and reduced d′ ($p < 0.05$, Wilcoxon signed-rank test, Figures 1G–1I).

Since activating PV or FoxP2 neurons during the stimulus presentation period increased lick rates in both Go and No-Go trials (Figures S1A–S1C and S1G–S1I), we next activated these neurons during the inter-trial interval (ITI) to determine whether the increased FA rate resulted from a direct effect on licking behavior. Compared to controls, activation of PV or FoxP2 neurons during the ITI did not significantly alter licking rates (Figures S1D–S1F and S1J–S1L), suggesting that the impaired task performance during stimulus-period activation was unlikely due to direct motor effects.

Inhibition of PV but not FoxP2 GPe neurons disrupts behavioral performance

We next performed experiments to inhibit PV or FoxP2 neurons during the stimulus presentation period, by injecting AAV-DIO-NpHR into the GPe of PV-Cre or FoxP2-Cre mice. In vivo recordings confirmed that NpHR activation effectively suppressed GPe neuron firing (Figures S2A and S2B). Compared to control mice, inhibition of PV neurons significantly increased the FA rate and decreased d′ ($p < 0.001$, Wilcoxon rank-sum test, Figures 2A–2D), whereas inhibition of FoxP2 neurons had no effect on behavioral performance ($p > 0.5$, Wilcoxon rank-sum test, Figures 2E–2H). Lick rate analysis showed that inhibiting PV neurons during the stimulus presentation period increased licking in No-Go trials (Figures S2C–S2E), whereas inhibiting FoxP2

neurons had no effect on licking (Figures S2I–S2K). To test whether this effect was due to a direct influence on licking behavior, we inhibited PV neurons during the ITI. Under this condition, the NpHR group did not show an increased lick rate compared to controls (Figures S2F–S2H). These results suggest that the increased FA rate and decreased d′ observed with inhibiting PV neuron were not attributable to direct modulation of licking movements.

Thus, although activating PV and FoxP2 neurons both disrupted behavioral performance, only PV neurons played an essential role in suppressing inappropriate responses in the Go/No-Go visual task.

Optogenetic tagging of GPe PV and FoxP2 neurons

To identify GPe PV and FoxP2 neurons for subsequent analysis of task-related activity, we performed optogenetic tagging during electrophysiological recordings using an optotrode in PV-Cre or FoxP2-Cre mice, in which AAV-FLEX-ChrimsonR was injected into the GPe (Figures 3A and 3C). Neurons were identified as ChrimsonR-expressing based on two criteria:[42,43] (1) significant activation by laser stimulation with a short latency (within 6 ms), and (2) a Pearson's correlation coefficient > 0.95 between laser-evoked and spontaneous spike waveforms (Figures 3B and 3D).

Depending on the latency threshold applied (1–6 ms), we identified 25–153 PV neurons out of 895 recorded units in PV-Cre mice, and 26–137 FoxP2 neurons out of 1606 units in FoxP2-Cre mice (Figures 3E and S3A). At thresholds between 2 and 4 ms, PV neurons exhibited higher spontaneous firing rates and narrower spike waveform

peak widths compared to FoxP2 neurons (Figures 3F, 3G, and S3B), consistent with previous reports.[15,24,44,45] For subsequent analyses, we adopted a 3 ms latency threshold, which provided a more stringent classification of ChrimsonR-expressing cells while retaining a sufficient number of neurons for statistical analysis.

Distinct task-related activity patterns in GPe PV and FoxP2 neurons

We next analyzed task-modulated GPe PV and FoxP2 neurons (three-way ANOVA, $p < 0.01$; see Methods). These neurons exhibited diverse firing patterns that were time-locked to key task events, including stimulus onset, lick-bout onset and offset, and outcome onset. Example spike rasters and corresponding peristimulus time histograms (PSTHs) are shown in the top and middle rows of Figures 4B and 4C, respectively. To disentangle the contributions of each task event to neuronal activity, we fitted the responses of task-modulated neurons using a generalized linear model (GLM).[46] The model included regressors for stimuli (Go and No-Go), licking events (lick-bout onset and offset), and outcomes (Hit, CR, and FA) (Figure 4A). Each regressor was represented by a set of time-lagged predictors, enabling the GLM coefficients to capture the temporal dynamics of task-related neuronal responses (Methods). For the example neurons (Figures 4B and 4C), the temporal profiles of GLM coefficients (bottom row) closely matched the corresponding PSTHs. Model performance was evaluated by computing the Pearson's correlation coefficient (CC) between the predicted and actual activity on held-out test data. CC values did not differ significantly between PV and FoxP2 neurons ($p = 0.66$, Wilcoxon rank-sum test; PV: 0.29 ± 0.02, $n = 51$; FoxP2: 0.30

± 0.02, mean ± SEM, n = 52) (Figure S3E). Moreover, the behavioral discrimination performance of PV-Cre and FoxP2-Cre mice during these electrophysiological recordings did not differ significantly (Figure S3D).

Figure 5A depicts the temporal profiles of GLM coefficients averaged across task-modulated PV neurons (blue) and FoxP2 neurons (brown). For sensory-related activity, both PV and FoxP2 neurons showed larger GLM coefficients for the Go than the No-Go stimulus regressor (Figures 5A and 5B). To quantify stimulus selectivity, we computed a cue selectivity index (cue SI) defined as $(\beta_{Go} - \beta_{No\text{-}Go})/(|\beta_{Go}| + |\beta_{No\text{-}Go}|)$, in which β_{Go} and $\beta_{No\text{-}Go}$ represent the average coefficients in the 0 – 0.5 s window after stimulus onset in Go and No-Go trials, respectively. Both PV and FoxP2 neurons had significantly positive cue SI values ($p < 0.01$, Wilcoxon signed rank test, Figure 5C, left), indicating a preference for visual stimulus associated with Go trials, and their cue SIs were not significantly different ($p = 0.16$, Wilcoxon rank-sum test, Figure 5C, left). Temporal analysis using a 0.1 s sliding window revealed that PV neurons displayed significantly higher cue SI values within 0.3 s after stimulus onset ($F_{(1, 101)} = 4.03$, $p = 0.047$, two-way ANOVA with mixed design, Figure 5C, right), suggesting enhanced stimulus selectivity during the early response phase.

For the lick-bout onset event, PV neurons exhibited a transient increase in GLM coefficients, whereas FoxP2 neurons showed a sustained increase, with values significantly higher than those of PV neurons ($F_{(15, 1515)} = 6.23$, $p_{interaction} = 0.0026$, two-way ANOVA with mixed design, Figure 5A). Following lick-bout offset, PV neurons displayed sustained negative coefficients, while FoxP2 neurons initially maintained

positive coefficients for a short period before gradually transitioning to negative values (Figure 5A). These results reveal distinct temporal dynamics in licking-related activity between PV and FoxP2 neurons.

Next, we analyzed outcome-related activity. GLM coefficients were markedly elevated in Hit trials but were low in CR and FA trials (Figure 5A). In Hit trials, PV neurons showed a transient increase in coefficients immediately following reward delivery, with a peak amplitude greater than that of FoxP2 neurons ($F_{(10, 1010)} = 3.79$, $p_{interaction} = 0.017$, two-way ANOVA with mixed design, Figure 5A). To quantify outcome selectivity, we calculated an outcome selectivity index (outcome SI) (Figure 5E), defined as $(\beta_{Hit} - \beta_{FA})/(|\beta_{Hit}| + |\beta_{FA}|)$, where β_{Hit} and β_{FA} represent the average coefficients in the 0 – 1 s window in Hit and FA trials, respectively. PV neurons exhibited significantly positive outcome SI values ($p = 0.016$, Wilcoxon signed-rank test, Figure 5D, left), whereas the outcome SI of FoxP2 neurons did not differ significantly from zero ($p = 0.43$, Wilcoxon signed-rank test, Figure 5D, left). A sliding-window analysis over the 1 s following reward delivery revealed that PV neurons had significantly higher outcome SI values than FoxP2 neurons at multiple time points during the early outcome period ($F_{(10, 1010)} = 4.31$, $p_{interaction} = 0.0018$, two-way ANOVA with mixed design, Figure 5D, right), indicating stronger selectivity for rewarded over unrewarded outcomes in PV neurons.

To validate the GLM results, we plotted the Z-scored PSTHs averaged across all PV neurons and across all FoxP2 neurons, aligned to each task event (Figure S4). The average activity profiles recapitulated the differences observed in the GLM coefficients

between the two cell types. Similar distinctions between PV and FoxP2 neurons were also evident when neurons were identified using either the 2 ms or 4 ms latency threshold (Figure S5), confirming that these effects were robust across classification criteria. Together, the results demonstrate that while both PV and FoxP2 neurons encoded task-relevant events, sliding-window analyses revealed that PV neurons exhibited higher selectivity for visual stimuli and reward outcomes during early task epochs, while FoxP2 neurons showed more sustained activity related to licking behavior.

The activity patterns of PV and FoxP2 neurons may be shaped by their afferent inputs. To investigate this, we mapped monosynaptic inputs to these GPe neuron types using PV-Cre and FoxP-Cre mice. A Cre-dependent helper virus (AAV2/9-hSyn-FLEX-mCherry-2A-TVA-2A-RVG-WPRE-pA) was injected into the GPe, followed by a modified rabies virus (RV-EnvA-ΔG-EGFP) (Figure S6A). Because PV is also expressed in thalamic reticular nucleus[47] and FoxP2 in the striatum,[25] we used a small injection volume of the helper virus to ensure that most starter cells were confined to the GPe (Figures S6B and S6E). Automated 3D reconstruction[48] revealed that PV neurons received widespread inputs from the striatum, cortex (e.g., secondary motor area), and thalamus (e.g., posterior complex of the thalamus and parafascicular nucleus) (Figures S6C and S6D). Inputs to FoxP2 neurons were detected in the striatum (Figure S6F), with occasional sparsely labeled cells detected in other regions, including the STN, primary somatosensory area, and temporal association areas (Figure S6G), likely reflecting the limited number of starter cells in the GPe.

Impact of GPe PV neuron activity on task-related responses in the SNr

Previous studies have shown that manipulating GPe PV neurons can modulate pathological burst spiking in SNr neurons in a mouse model of PD.[26] How GPe PV neurons influence task-related activity in the SNr under physiological conditions remains unclear. Given their essential role in the Go/No-Go visual task (Figure 2), we next investigated whether and how GPe PV activity shapes sensorimotor signaling in the SNr. To this end, we expressed NpHR in GPe PV neurons of PV-Cre mice and performed extracellular recordings in the SNr following task training (Figures 6A and S7A). Putative GABAergic SNr units were identified based on their spike waveforms[49] (Figure S7B), and neurons with baseline firing rates exceeding 5 Hz were included in the analyses.

In these mice, inactivation of GPe PV neurons significantly increased the FA rate ($p = 2.4\times10^{-4}$, Wilcoxon signed rank test) and decreased d' ($p = 2.4\times10^{-4}$, n = 13 sessions from 4 mice, Wilcoxon signed rank test, Figure 6B). At the neuronal level, 39.4% (74/188) of SNr neurons exhibited a significant increase in mean firing rate following inactivation of GPe PV neurons, while 46.8% (88/188) showed a significant decrease (Figure 6C, S7C, and S7D). Considering SNr neurons receive inputs from the GPe as well as other brain regions,[20,50-52] we focused our subsequent analyses on those SNr neurons with significant response changes, which are more likely to receive direct input from the GPe. To dissect how GPe PV neuron activity modulates task-related responses in these SNr neurons (two example neurons are shown in Figures 6D and 6E), we

performed separate GLM analyses under laser-off and laser-on conditions for each neuron.

Among SNr neurons with increased firing rate during GPe PV inactivation, stimulus-related coefficients for both Go and No-Go cues were enhanced (Figure 7A). Cue SI was significantly reduced, both when computed from the average GLM coefficients in the 0 – 0.5 s window after stimulus onset ($p = 9.6\times10^{-7}$, n = 74, Wilcoxon signed-rank test, Figure 7C, left) and when assessed using sliding-window analysis over time ($F_{(1, 73)} = 52.37$, $p = 3.79\times10^{-10}$, two-way repeated measures ANOVA, Figure 7C, right). These neurons also showed a more negative coefficient for lick-bout offset under laser-on compared to laser-off conditions ($F_{(1, 73)} = 9.02$, p = 0.0036, two-way repeated measures ANOVA, Figure 7A; p = 0.025, two-way repeated measures ANOVA followed by Sidak's multiple comparisons test, Figure 7B), whereas the coefficient for lick-bout onset remained unchanged (Figures 7A and 7B). In contrast, outcome-related coefficients were not significantly affected (Figure 7A). While the difference in outcome SI between laser-on and laser-off conditions was statistically significant in the sliding-window analysis ($F_{(1, 73)} = 4.67$, p = 0.034, two-way repeated measures ANOVA, Figure 7D, right), the magnitude of this effect was small.

For SNr neurons with decreased firing rate during GPe PV inactivation, stimulus encoding remained unchanged (Figure 7E), and cue SI showed no significant difference in the 0 – 0.5 s average, with a modest change over time (Figure 7G). In contrast, the coefficient for lick-bout onset increased significantly ($F_{(1, 87)} = 16.08$, $p = 1.28\times10^{-4}$, two-way repeated measures ANOVA, Figure 7E; $p = 8.95\times10^{-4}$, two-way repeated

measures ANOVA followed by Sidak's multiple comparisons test, Figure 7F), while the lick-bout offset coefficient remained unaffected (Figures 7E and 7F). Notably, outcome-related coefficients for Hit, CR, and FA trials all decreased significantly under laser-on condition ($p < 0.01$, two-way repeated measures ANOVA, Figures 7E and 7F). Outcome SI, computed from the average GLM coefficients in the 0 – 1 s window after outcome onset, was significantly negative during laser-off ($p = 9.40\times10^{-5}$, Wilcoxon signed-rank test, Figure 7H, left) and shifted toward zero under laser-on, with a significant difference between conditions ($p = 2.90\times10^{-6}$, Wilcoxon signed-rank test, Figure 7H, left). Sliding-window analysis further revealed significant differences in outcome SI between laser-off and laser-on conditions ($F_{(1,87)} = 25.79$, $p = 2.15\times10^{-6}$, two-way repeated measures ANOVA, Figure 7H, right).

Together, these findings indicate that GPe PV neurons exert subpopulation-specific modulation in the SNr. Following inactivation of GPe PV neurons, cue selectivity was significantly reduced in SNr neurons with increased firing, while their outcome selectivity remained unchanged; in contrast, cue selectivity remained unchanged in SNr neurons with decreased firing, but their FA outcome preference was significantly diminished.

DISCUSSION

Using a Go/No-Go visual discrimination task, we found that while activation of both PV and FoxP2 neurons in the GPe altered behavior, only PV neurons were critical for task performance. Both cell types conveyed task-related signals, yet PV neurons

exhibited greater selectivity to visual cues and trial outcomes, while FoxP2 neurons showed more prolonged activity associated with licking behavior. Monosynaptic input mapping showed that PV neurons received diverse inputs from cortical, striatal, and thalamic regions. Furthermore, inactivating GPe PV neurons disrupted stimulus selectivity and outcome representations in downstream SNr neurons. These findings reveal the specific roles of GPe PV and FoxP2 neurons in regulating the flow of sensory, motor, and outcome information in the BG during goal-directed sensorimotor behavior.

Contribution of GPe specific cell types to behavioral performance

Previous studies have shown that activation of GPe PV neurons enhanced movement in healthy mice and restored mobility in PD mouse model,[18,20,26,53] while their inactivation did not affect movement under dopamine-depleted conditions.[26] Moreover, selective activation and inhibition of GPe PV neurons projecting to the SNr increased and decreased locomotor activity, respectively.[22] Activating GPe FoxP2 or Npas1 neurons, on the other hand, suppressed locomotion.[20,24,25]

In the present study, we used both gain- and loss-of-function approaches to dissect the roles of GPe PV and FoxP2 neurons in perceptual decision-making. Activating either population during stimulus presentation period led to increased FA rates and reduced d′, suggesting that both can perturb behavior when artificially driven. However, only PV neuron inactivation produced similar impairments, highlighting their essential role in accurate sensorimotor decision-making. Importantly, activation or inactivation of these neurons during ITI did not produce significant increases in licking behavior

compared to controls (Figures S1 and S2), suggesting that the behavioral impairments were not due to changes in motor output per se, but rather a disruption of task-relevant sensory or decision-related processing. These findings support the growing view that GPe neurons participate in both motor and non-motor functions.[30,36,54] GPe PV neurons consist of distinct subpopulations projecting to the STN/SNr or PF,[5,22] though whether each contributes to task performance remains to be determined.

Previous studies showed that inhibiting GPe Npas1 neurons increased movement,[20] and that GPe arkypallidal neurons were involved in canceling imminent action during a stop-signal task.[21] However, in our study, inactivation of GPe FoxP2 neurons—a subpopulation of Npas1 neurons—did not affect licking behavior or behavioral performance in the Go/No-Go task (Figures 2 and S2). This suggests that the role of GPe FoxP2 neurons in motor or cognitive control may depend on the specific behavioral context or task demands.

Task-relevant encoding and input sources of GPe PV and FoxP2 neurons

In vivo whole-cell recordings from anesthetized mice revealed that arkypallidal and prototypic GPe neurons displayed distinct multiphasic response patterns to whisker stimulation via air puff.[39,40] In rats performing a novel environment exposure task, population activity of GPe neurons encoded environmental identity,[55] suggesting that specific GPe neurons discriminate sensory features of the surroundings. Building on these studies, we applied GLM analysis to isolate stimulus-related activity and found that GPe PV neurons exhibited stronger stimulus selectivity compared to FoxP2

neurons. The stronger stimulus selectivity of PV neurons may reflect their preferential role in supporting task-relevant sensory processing, consistent with the observation that only their inhibition disrupted performance in the Go/No-Go visual discrimination task. Given that the Go stimulus predicted reward while the No-Go stimulus did not, the preference of PV neurons for the Go stimulus may also reflect encoding of reward expectation. These observations are consistent with findings in rats, where faster-firing GPe PV neurons were more strongly modulated by value than arkypallidal neurons,[34] and with primate studies reporting that high-frequency discharge GPe neurons exhibited selective responses to reward-predicting cues.[33,56]

Fiber photometry recordings showed that GPe PV and Npas1 neurons increased activity at locomotion onset.[22,25] In vivo extracellular recordings from moving mice revealed heterogeneous activity patterns among prototypic GPe neurons during movement, whereas FoxP2-expressing arkypallidal GPe neurons exhibited firing rate increases at movement onset, with both cell types reliably encoding movement.[15] Consistent with these findings, we found that FoxP2 neurons displayed a more sustained increase in firing rate following lick-bout onset, whereas PV neurons showed more transient increases. At lick-bout offset, FoxP2 neurons showed a gradual transition from positive to negative GLM coefficients. This pattern suggests that FoxP2 neurons could contribute to representing ongoing orofacial motor activity throughout the licking period.

Beyond sensory and motor processing, GPe neurons are also implicated in encoding reward-related information, including reward outcome, prediction, and

value.[31-34,56-58] Consistent with findings in monkey demonstrating GPe neuron responses to reward outcomes,[56] we observed significant modulation of PV and FoxP2 neuron activity around the time of Hit outcomes, with PV neurons exhibiting stronger responses. Moreover, the two cell types exhibited distinct temporal profiles of outcome selectivity aligned to outcome onset. The mechanisms underlying these cell type-specific differences in reward-related activity and their functional implications remain to be explored.

Retrograde tracing studies have shown that GPe neurons receive inputs from diverse brain regions, including the striatum, STN, thalamus, cortex, amygdala, hypothalamus, and midbrain regions.[19,22,28,37,59-63] Consistent with these reports, we found that GPe PV neurons were innervated by striatal, cortical, thalamic, and midbrain areas. Their task-related activity likely reflects integrated input from these sources: stimulus selectivity may arise from cortical or thalamic input (e.g., secondary motor cortex and parafascicular nucleus),[64,65] motor-related activity from STN or motor cortex,[66] and outcome responses from midbrain signals.[67] These possibilities highlight the GPe as a key node for integrating sensory, motor, and reward signals to support goal-directed behavior. Further studies are required to delineate how each input contributes to the dynamic activity of GPe PV neurons during behavior.

GPe modulation of SNr activity

A recent study demonstrated that optogenetic stimulation of GPe PV neurons caused heterogeneous changes in spontaneous firing rates of SNr neurons, with a large fraction

exhibiting reduced firing rates and a small subset showing increased activity.[68] In dopamine-depleted mice, optogenetic stimulation of GPe PV neurons attenuated pathological activity in the SNr by reducing the proportion of bursting neurons.[26] In monkeys performing a sequential saccade choice task, blocking GABAergic inputs to GPe with bicuculine impaired the suppression of saccades to low-value objects and reduced the excitatory responses of SNr neurons to these objects, without affecting SNr responses to high-value objects.[69] Building on these findings, we sought to directly examine how GPe PV neuron activity influences SNr neural responses during behavior. We found that optogenetic inactivation of GPe PV neurons caused bidirectional changes in SNr firing rates across distinct neuron populations, modulating responses related to stimuli, licking, and outcomes. The observed decreases in firing rate may reflect intra-SNr inhibitory interactions through axon collaterals.[70-72] This heterogenous changes in SNr firing rates aligns with previous findings that manipulating striatal D2-MSNs can produce both increases and decreases in SNr activity.[42,73] Notably, inactivation of GPe PV neurons weakened cue selectivity in SNr neurons with increased firing and attenuated outcome selectivity in those with decreased firing. These results suggest that under normal conditions, GPe PV neuron activity sharpens the encoding of stimulus and outcome information in distinct SNr subpopulations, thereby supporting the transmission of task-relevant signals through the basal ganglia output.

Limitations of the study

The GPe PV neurons identified in our study likely included heterogeneous subtypes projecting to distinct downstream targets, including the STN, SNr, and PF.[5,22]

Further work is needed to dissect the specific sensorimotor roles of these PV neuron subtypes during perceptual decision-making. Although our GLM analysis included regressors related to licking movements, we did not monitor head or body motions in head-fixed mice.[74] In future studies, it would be of great interest to investigate how distinct GPe cell types integrate sensory information with a broader repertoire of motor signals.

RESOURCE AVAILABILITY

Lead contact

Further information and requests for resources and reagents should be directed to and will be fulfilled by the lead contact, Haishan Yao (haishanyao@ion.ac.cn).

Materials availability

This study did not generate new unique reagents.

Data and code availability

- The data described in this paper have been deposited at Mendeley Data and are publicly available as of the date of publication. Accession numbers are listed in the key resources table.
- All original code has been deposited at Mendeley Data and is publicly available as of the date of publication. Accession numbers are listed in the key resources table.
- Any additional information required to reanalyze the data reported in this paper is available from the lead contact upon request.

ACKNOWLEDGMENTS

This work was supported by the STI2030-Major Projects (2021ZD0203700/2021ZD0203703), the Strategic Priority Research Program of the Chinese Academy of Sciences (Grant No. XDB1010201), and the National Natural Science Foundation of China (31771151 and 32171030 to H.Y., 32100829 to D.L.).

AUTHOR CONTRIBUTIONS

X.P., D.L., and H.Y. conceived and designed the project. X.P. performed the majority of the experiments and data analyses. D.L. conducted the SNr recordings and RV tracing experiments. J.R. and T.X. developed the GLM analysis code. K.Z., J.X. assisted with behavioral training. Y. L. helped with virus injection and spike sorting. H.Y. wrote the manuscript, with feedback from all authors.

DECLARATION OF INTERESTS

The authors declare no competing interests.

FIGURE LEGENDS

Figure 1. Activation of PV or FoxP2 GPe neurons impairs performance in the Go/No-Go visual task

(A) Schematic of the trial structure.

(B) Left, representative fluorescence image showing AAV-FLEX-ChrimsonR expression in the GPe of a PV-Cre mouse. Right, lick rasters from an example PV-Cre mouse during laser-off and laser-on trials. For display purposes, 100 laser-off trials and 100 laser-on trials were shown in the raster plot. Shading, duration of laser stimulation.

(C) Left, representative fluorescence image showing AAV-FLEX-ChrimsonR expression in the GPe of a FoxP2-Cre mouse. Right, lick rasters from an example FoxP2-Cre mouse during laser-off and laser-on trials (100 trials were shown for each condition). Shading, duration of laser stimulation.

(D) Top, Hit rates in laser-off and laser-on trials for control (n = 5) and ChrimsonR (n = 6) PV-Cre mice. * p = 0.031, Wilcoxon signed-rank test. Bottom, comparison of ΔHit rate between control and ChrimsonR PV-Cre mice. p = 0.056, Wilcoxon rank-sum test.

(E) Same as (D), but for FA rates in GFP and ChrimsonR PV-Cre mice. Top, * p = 0.031, Wilcoxon signed-rank test. Bottom, ** p = 0.0043, Wilcoxon rank-sum test.

(F) Same as (D), but for d′ in GFP and ChrimsonR PV-Cre mice. Top, * p = 0.031, Wilcoxon signed-rank test. Bottom, ** p = 0.0043, Wilcoxon rank-sum test.

(G) Top, Hit rates in laser-off and laser-on trials for control (n = 6) and ChrimsonR (n = 6) FoxP2-Cre mice. Bottom, comparison of ΔHit rate between control and ChrimsonR FoxP2-Cre mice. p = 0.97, Wilcoxon rank-sum test.

(H) Same as (G), but for FA rates in GFP and ChrimsonR FoxP2-Cre mice. Top, * p = 0.031, Wilcoxon signed-rank test. Bottom, ** p =0.0022, Wilcoxon rank-sum test.

(I) Same as (G), but for d′ in GFP and ChrimsonR FoxP2-Cre mice. Top, * p = 0.031, Wilcoxon signed-rank test. Bottom, ** p =0.0022, Wilcoxon rank-sum test.

Scale bars, 200 μm. Data represent mean ± SEM.

See also Figure S1.

Figure 2. Inactivation of PV but not FoxP2 GPe neurons impairs performance in the Go/No-Go visual task

(A) Left, representative fluorescence image showing AAV-DIO-NpHR expression in the GPe of a PV-Cre mouse. Right, lick rasters from an example PV-Cre mouse in laser-off and laser-on trials. For display purposes, 100 laser-off trials and 100 laser-on trials were shown in the raster plot. Shading, duration of laser stimulation.

(B) Top, Hit rates in laser-off and laser-on trials for control (n = 7) and NpHR (n = 8) PV-Cre mice. Bottom, comparison of ΔHit rate between control and NpHR PV-Cre mice. p = 0.34, Wilcoxon rank-sum test.

(C) Same as (B), but for FA rates in GFP and NpHR PV-Cre mice. Top, ** p = 0.008, Wilcoxon signed-rank test. Bottom, *** $p = 3.11\times10^{-4}$, Wilcoxon rank-sum test.

(D) Same as (B), but for d′ in GFP and NpHR PV-Cre mice. Top, ** p = 0.008, Wilcoxon signed-rank test. Bottom, *** $p = 3.11\times10^{-4}$, Wilcoxon rank-sum test.

(E) Left, representative fluorescence image showing AAV-DIO-NpHR expression in the GPe of a FoxP2-Cre mouse. Right, lick rasters from an example FoxP2-Cre mouse in laser-off and laser-on trials (100 trials were shown for each condition). Shading, duration of laser stimulation.

(F) Top, Hit rates in laser-off and laser-on trials for control (n = 7) and NpHR (n = 10) FoxP2-Cre mice. Bottom, p = 0.87, Wilcoxon rank-sum test.

(G) Same as (F), but for FA rates in GFP and NpHR FoxP2-Cre mice. Bottom, p = 0.96, Wilcoxon rank-sum test.

(H) Same as (F), but for d′ in GFP and NpHR FoxP2-Cre mice. Bottom, p = 0.74,

Wilcoxon rank-sum test.

Scale bars, 200 μm. Data represent mean ± SEM.

See also Figure S2.

Figure 3. Identification of PV or FoxP2 GPe neurons

(A) Fluorescence image showing AAV-FLEX-ChrimsonR-tdTomato expression in the GPe of a PV-Cre mouse. Green, electrode track labeled with DiO.

(B) Spike rasters (left) and PSTH (right) of an identified PV neuron. Time 0 marks laser onset. Red shading, laser stimulation. Inset, average spike waveforms recorded during laser-off and laser-on trials.

(C) Fluorescence image showing AAV-FLEX-ChrimsonR-tdTomato expression in the GPe of a FoxP2-Cre mouse. Green, electrode track labeled with DiO.

(D) Spike rasters (left) and PSTH (right) of an identified FoxP2 neuron (format as in B).

(E) Fraction of identified PV and FoxP2 GPe neurons using latency threshold ranging from 1 to 6 ms. PV neurons were identified from a total of 895 units in 50 sessions of 8 PV-Cre mice. FoxP2 neurons were identified from a total of 1606 units in 85 sessions of 14 FoxP2-Cre mice.

(F) Comparison of spike rates between PV neurons (n = 76) and FoxP2 GPe neurons (n = 76) identified using a 3-ms latency threshold. *p = 0.048, Wilcoxon rank-sum test.

(G) Comparison of spike peak width (the width at half-maximum of the waveform peak amplitude) between PV and FoxP2 GPe neurons identified using a 3-ms latency threshold. *p = 0.036, Wilcoxon rank-sum test.

Scale bars, 200 μm.

See also Figure S3.

Figure 4. GLM analysis of task-related activity in example GPe neurons

(A) Schematic of the GLM framework, showing task-related variables and their corresponding weights.

(B) Spike rasters (top), PSTHs (middle), and GLM coefficients (bottom) from an example PV neuron, aligned to different task events: stimulus onset (Go and No-Go), lick-bout onset and offset, and outcome events (Hit: reward onset, CR: end of response window, FA: onset of sound cue triggered by the first lick in FA trials). For display purposes, 80 Go trials and 80 No-Go trials were shown in the raster plot; PSTHs and GLM coefficients were computed from all trials.

(C) Same as (B), but for an example FoxP2 neuron.

Figure 5. Comparison of GLM coefficients between task-modulated PV and FoxP2 GPe neurons

(A) Temporal profiles of GLM coefficient averaged across task-modulated PV neurons (n = 51) or FoxP2 neurons (n = 52) for each regressor. Horizontal ticks indicate time points where GLM coefficients differed significantly between PV and FoxP2 neurons ($p < 0.05$), determined by a two-way ANOVA with mixed design followed by Tukey's multiple comparisons test. For each regressor, the two-way ANOVA was applied only to time points within specified time windows: Go or No-Go

stimulus, 0 – 0.5 s; lick-bout onset, 0 – 1.5 s; lick-bout offset, 0 – 1.5 s; Hit, 0 – 1 s; CR, -1 – 0 s (with time zero defined as the end of the answer period); and FA, 0 – 1 s.

(B) Mean GLM coefficients averaged over defined time windows. *$p < 0.05$, **$p < 0.01$, two-way ANOVA with mixed design followed by Tukey's multiple comparisons test.

(C) Left, cue SI of PV and FoxP2 GPe neurons. **$p < 0.01$, ***$p < 0.001$, Wilcoxon signed-rank test. Right, temporal dynamics of cue SI for PV and FoxP2 neurons. *$p < 0.05$, two-way ANOVA with mixed design ($F_{(1, 101)} = 4.03$, $p = 0.047$) followed by Tukey's multiple comparisons test.

(D) Left, outcome SI of PV and FoxP2 GPe neurons. * $p < 0.05$, Wilcoxon signed-rank test. Right, temporal dynamics of outcome SI for PV and FoxP2 neurons. * $p < 0.05$, two-way ANOVA with mixed design ($F_{(10, 1010)} = 4.31$, $p_{interaction} = 0.0018$) followed by Tukey's multiple comparisons test.

PV neurons and FoxP2 neurons were identified using a latency threshold of 3 ms. Data represent mean ± SEM.

See also Figures S4, S5, and S6.

Figure 6. SNr neuronal activity during inactivation of PV GPe neurons

(A) Left, schematic of SNr recording combined with GPe PV neuron inactivation. Right, example fluorescence image showing electrode track labeled with DiI in SNr. Scale bar, 200 μm.

(B) In PV-Cre mice used for SNr recordings, inactivation of GPe PV neurons significantly increased FA rate and decreased d'. n = 13 sessions. *** $p < 0.001$, Wilcoxon signed-rank test.

(C) Pie chart showing proportions of SNr neurons (n = 188) with significantly increased, decreased, or unchanged firing rates after inactivation of GPe PV neurons.

(D) Spike rasters and PSTHs of an example SNr neuron with a significant increase in mean firing rate after inactivation of GPe PV neurons. For display purposes, 50 – 60 Go trials and 50 – 60 No-Go trials were shown in the raster plot; PSTHs were computed from all trials.

(E) Same as (D), but for an example SNr neuron with a significant decrease in mean firing rate following GPe PV neuron inactivation.

Figure 7. Effect of inactivating PV GPe neurons on GLM coefficients and selectivity of SNr neurons

(A–D) SNr neurons with significantly increased firing rate (n = 74):

(A) Temporal profiles of GLM coefficients of each event under laser-off (black) and laser-on (green) conditions. Horizontal ticks indicate time points where GLM coefficients differed significantly between laser-off and laser-on conditions ($p < 0.05$), determined by a two-way repeated measures ANOVA followed by Sidak's multiple comparisons test. For each regressor, the two-way ANOVA was applied only to time points within specified time windows: Go or No-Go stimulus, 0 – 0.5 s; lick-bout onset, 0 – 1.5 s; lick-bout offset, 0 – 1.5 s; Hit, 0 – 1 s; CR, -1 – 0 s

(with time zero defined as the end of the answer period); and FA, 0 – 1 s.

(B) GLM coefficients averaged over defined time windows. *$p < 0.05$, ***$p < 0.001$, two-way repeated measures ANOVA ($F_{(3.06,\ 223.1)} = 4.94$, $p_{interaction} = 0.0023$) followed by Sidak's multiple comparisons test.

(C) Left, cue SI computed using GLM coefficients (Go and No-Go) averaged over 0 – 0.5 s. ***$p < 0.001$, Wilcoxon signed-rank test. Right, temporal dynamics of cue SI. *$p < 0.05$, two-way repeated measures ANOVA ($F_{(1,73)} = 52.37$, $p = 3.79\times10^{-10}$) followed by Sidak's multiple comparisons test.

(D) Left, outcome SI computed using GLM coefficients (Hit and FA) averaged over 0 – 1 s. **$p < 0.01$, Wilcoxon signed-rank test. Off vs On: $p = 0.051$, Wilcoxon signed-rank test. Right, temporal dynamics of outcome SI. $F_{(1,\ 73)} = 4.67$, $p = 0.034$, two-way repeated measures ANOVA.

(E–H) SNr neurons with significantly decreased firing rate (n = 88):

(E) Temporal profiles of GLM coefficients of each event under laser off and laser on conditions, as described in (A).

(F) GLM coefficients averaged over defined time windows. **$p < 0.01$, ***$p < 0.001$, two-way repeated measures ANOVA ($F_{(1,87)} = 15.42$, $p = 1.72\times10^{-4}$) followed by Sidak's multiple comparisons test.

(G) Left, cue SI computed using GLM coefficients (Go and No-Go) averaged over 0 – 0.5 s. ***$p < 0.001$, Wilcoxon signed-rank test. Off vs On: $p = 0.098$, Wilcoxon signed-rank test. Right, temporal dynamics of cue SI. $F_{(4.32,375.9)} = 3.28$, $p_{interaction} = 0.0096$, two-way repeated measures ANOVA.

(H) Left, outcome SI computed using GLM coefficients (Hit and FA) averaged over 0 – 1 s. ***$p < 0.001$, Wilcoxon signed-rank test. Right, temporal dynamics of outcome SI. *$p < 0.05$, two-way repeated measures ANOVA ($F_{(1,87)} = 25.79$, $p = 2.15\times10^{-6}$) followed by Sidak's multiple comparisons test.

Data represent mean ± SEM.

See also Figure S7.

STAR METHODS

KEY RESOURCES TABLE

REAGENT OR RESOURCE	SOURCE	IDENTIFIER
Antibodies		
rabbit anti-GFP	Invitrogen	G10362
donkey anti-rabbit Alexa Fluor	Invitrogen	A21206
goat anti-rabbit Alexa Fluor	Invitrogen	A21245
Bacterial and virus strains		
AAV2/9-hSyn-FLEX-ChrimsonR-tdTomato-WPRE-PA	Shanghai Taitool Bioscience Co., Ltd.	S0186-9
AAV2/9-hSyn-DIO-ChrimsonR-mCherry-WPRE-hGHpA	Wuhan BrainVTA Co., Ltd.	N/A
AAV2/5-EF1α-DIO-eNpHR3.0-EYFP-WPRE-hGHpA	Wuhan BrainVTA Co., Ltd.	N/A
AAV5-EF1α-DIO-eNpHR3.0-EYFP	Addgene	26966
AAV2/5-CAG-FLEX-EGFP-WPRE-pA	Shanghai Taitool Bioscience Co., Ltd.	N/A
AAV2/9-hSyn-FLEX-mCherry-2A-TVA-2A-RVG-WPRE-pA	Shanghai Taitool Bioscience Co., Ltd.	S0380-9-H50
RV-EnvA-ΔG-EGFP	Shenzhen BrainCase Co., Ltd.	BC-RV211115
Chemicals, peptides, and recombinant proteins		

Xylazine	Dunhua Shengda Animal Pharmaceutical	N/A
Zoletil	Virbac	N/A
Lincomycin hydrochloride–lidocaine hydrochloride gel	Jiangxi Decheng Pharmaceutical	N/A
Isoflurane	RWD Life Science	R510-22
DAPI Fluoromount-G	SouthernBiotech	0100-20
DiO / DiI	Invitrogen	D282 or D275
Rimadyl	Pfizer	N/A
Deposited data		
Datasets	This paper	Mendeley Data: https://doi.org/10.17632/z6sg8rzhxb.1
Analysis code	This paper	Mendeley Data: https://doi.org/10.17632/z6sg8rzhxb.1
Experimental models: Organisms/strains		
Mouse: PV-Cre	The Jackson Laboratory	stock No. 008069
Mouse: FoxP2-Cre	The Jackson Laboratory	stock No. 030541
Software and algorithms		
Offline Sorter	Plexon	https://plexon.com
MATLAB	Mathworks	https://www.mathworks.com
Graphpad Prism 8	GraphPad Software	https://www.graphpad.com/
ImageJ	NIH	https://imagej.net/ij
AMaSiNe	Song et al., Cell Reports, 2020	https://github.com/vsnnlab/AMaSiNe

EXPERIMENTAL MODEL AND SUBJECT DETAILS

Animals

All animal procedures (IACUC No. NA-013-2022) were approved by the Animal Care and Use Committee at the Center for Excellence in Brain Science and Intelligence Technology (the Institute of Neuroscience), Chinese Academy of Sciences, and were conducted in accordance with the Center's guidelines for the care and use of laboratory animals. PV-Cre (The Jackson Laboratory, Bar Harbor, ME, USA, stock No. 008069) and FoxP2-Cre (The Jackson Laboratory, Bar Harbor, ME, USA, stock No. 030541) mice were used in the experiments. Adult (2 – 4 months old) mice of both sexes were used for the experiments. Mice were housed under standardized conditions (temperature: 22–23 °C, humidity: 40–70 %, 12-hour light/12-hour dark cycle) in the Center's animal facility.

METHOD DETAILS

Surgery and virus injection

The mice were anesthetized via intraperitoneal injection of a mixture of xylazine (40 mg/kg) and zoletil (30 mg/kg), then placed in a stereotaxic apparatus. The scalp was shaved, and lincomycin hydrochloride–lidocaine hydrochloride gel was applied to the incision site. A unilateral craniotomy (~ 0.5 mm diameter) was made above the targeted virus injection site. The virus (AAV: 3 – 5×10^{12} viral particles/mL, rabies virus: 4×10^{8} viral particles/mL) was injected using a glass pipette (10 – 20 μm tip diameter) connected to a syringe pump (Harvard Apparatus, Holliston, MA, USA) at a rate of 100

nL/min. After completion of virus injection, the pipette was left in place for at least 10 min before being removed.

To activate GPe PV or FoxP2 neurons, 100 nL of AAV2/9-hSyn-FLEX-ChrimsonR-tdTomato-WPRE-PA was injected at a depth of 3400 μm into the GPe (AP -0.4 mm, ML 2.13 mm) of PV-Cre or FoxP2-Cre mice. An optic fiber (200 μm diameter, NA 0.5) was implanted 450 μm above the virus injection site in GPe. For inactivation of GPe PV (FoxP2) neurons, 200 (120) nL of AAV2/5-EF1α-DIO-eNpHR3.0-EYFP-WPRE-hGHpA or AAV5-EF1α-DIO-eNpHR3.0-EYFP was injected at a depth of 3250 μm into the GPe of PV-Cre (FoxP2-Cre) mice. An optic fiber (400 μm diameter, NA 0.5) was implanted approximately 350 μm above the virus injection site in GPe. In control PV-Cre (FoxP2-Cre) mice, 200 (120) nL of AAV2/5-CAG-FLEX-EGFP-WPRE-pA was injected into the GPe. For optogenetic tagging of PV or FoxP2 neurons, 200 nL of AAV2/9-hSyn-FLEX-ChrimsonR-tdTomato-WPRE-PA or AAV2/9-hSyn-DIO-ChrimsonR-mCherry-WPRE-hGHpA was injected at a depth of 3400 μm into the GPe of PV-Cre or FoxP2-Cre mice. For behavioral experiments, a stainless-steel headplate was implanted and secured to the skull with dental cement. For extracellular recordings, the skull surface above the GPe or SNr (AP -3.16 mm, ML 1.30 mm) was marked with permanent ink. After surgery, lincomycin hydrochloride – lidocaine hydrochloride gel was applied to the incision site to prevent infection and relieve local pain. Mice were then given Rimadyl via their drinking water for 3 days for systemic analgesia, and were allowed to recover for at least 10 days before behavioral training.

For retrograde monosynaptic tracing,[75,76] 50 nL of AAV2/9-hSyn-FLEX-mCherry-2A-TVA-2A-RVG-WPRE-pA (for the expression of mCherry, TVA receptor, and rabies glycoprotein RVG) was injected at a depth of 3500 μm into the GPe of PV-Cre mice (AP -0.2 to -0.4 mm, ML 2.15 to 2.2 mm) or FoxP2-Cre mice (AP -0.4 mm, ML 2.15 mm). After 7 – 12 days, 200 nL of pseudotyped, glycoprotein-deficient rabies virus RV-EnvA-ΔG-EGFP was injected at the same site. One week later, the mice were euthanized, and histology experiments were performed.

Behavioral task

Visual stimuli used in the Go/No-Go task were oriented gratings (114° × 103°, contrast = 100%, spatial frequency = 0.04 cycles/deg), which were presented on a 19" LCD monitor (Dell P1917S, mean luminance 35–40 cd/m^2, refresh rate 60 Hz) placed 12 cm away from the eye contralateral to the virus injection site or the recording site. The Go stimulus (vertical grating) and No-Go stimulus (horizontal grating) were randomly interleaved. Each stimulus presentation period consisted of a waiting period, during which the grating was static, followed by an answer period, during which the vertical grating drifted rightward and the horizontal grating drifted upward.

Before training, mice were water-deprived for 2 days. During training, each mouse was head-fixed in a custom apparatus and placed in an acrylic tube inside the behavioral chamber. A lick spout was placed approximately 2 mm posterior to the mouse's nose tip and 1 mm below the lower lip. Licks were detected either using a custom-made electrical lick sensor or via the interruption of an infrared beam. Water was delivered

through a peristaltic pump (Kamoer, Shanghai, China). An Arduino-based microcontroller system was used for stimulus presentation, lick detection, water delivery, laser stimulation, and data acquisition. Task-related signals and lick signals were sampled at 1000 Hz.

Behavioral training consisted of three phases: habituation, conditioning, and visual discrimination. During the habituation phase (2 days), the mouse learned to lick the lickspout to receive a water reward (4 – 5 μL) delivered every 5 s. In the conditioning phase (2 days), a vertical grating was presented on each trial. The inter-trial interval began with a 4-s blank screen, followed by a variable blank period. During this period, the mouse was required to withhold licking for 3 s to terminate the trial. If a lick occurred during this period, the 3-s countdown was reset, extending the interval, until either the mouse successfully withheld licking for 3 s or the maximum duration of 13 s was reached. The presentation of the grating stimulus consisted of a 0.5-s waiting period followed by a 2.5-s answer period. A lick detected during the answer period triggered a water reward (4 – 5 μL). During the visual discrimination phase (7 – 21 days), the Go and No-Go trials were randomly interleaved. The timing of the waiting period, answer period, and inter-trial interval was the same as in the conditioning phase. In each trial, licking within the answer period were used to assess behavioral performance. In Go trials, licking within the answer period was rewarded with 4 – 5 μL of water (Hit), while no lick was counted as a Miss. In No-Go trials, licking during the answer period was considered a FA, and no lick was a correct rejection (CR). Each mouse performed the task for 1 – 1.5 h per session. For mice undergoing electrophysiological recording, the

first lick in the answer period of a No-Go trial triggered a sound cue (100 ms duration), which served as a temporal marker for the onset of FA events in the GLM analysis.

Optogenetic stimulation

Optical activation of NpHR was induced by green light, and activation of ChrimsonR was induced by red light. A green (532 nm) or a red (635 nm) laser (Shanghai Laser & Optics Century Co., Shanghai, China) was connected to an output optical fiber. Laser stimulation was controlled by an Arduino microcontroller. Laser was at a power of 5 – 20 mW and 0.5 – 2 mW at fiber tip for green and red laser, respectively.

For optogenetic activation (or inhibition) of PV or FoxP2 neurons, laser-off and laser-on blocks (20 trials/block) were interleaved within each session. When laser stimulation was applied during the stimulus presentation period, the laser was delivered from 0 to 3 s after stimulus onset in both Go and No-Go trials. For stimulation during the ITI, laser was applied for 2 s within the ITI.

Optogenetic tagging

For optogenetic tagging using PV-Cre or FoxP2-Cre mice, red laser stimulation (50 or 100 trials, each lasting 10 or 100 ms, with an inter-trial interval of 7–10 s) was delivered in the GPe through the optotrode fiber. Spike counts in the 1-s period preceding laser onset were compared with those in six post-laser windows, defined as the period from laser onset to 1, 2, 3, 4, 5, or 6 ms after onset, respectively. Each window was tested separately using a paired t-test, and a GPe unit was considered significantly activated

at a given latency if $p < 0.01$. Additionally, the Pearson's correlation coefficient between the spontaneous spike waveform and the laser-evoked spike waveform had to exceed 0.95 to confirm optogenetic tagging [42,43].

Extracellular recording

Mice trained in the Go/No-Go visual discrimination task for at least 7 days were used for extracellular recordings. Recordings were conducted in mice that maintained a d′ greater than 1.5 after 1 h of head-fixation. Prior to recording, mice were placed in an acrylic tube, and their headplates were fixed to a holder mounted on a stereotaxic apparatus. Anesthesia was induced with isoflurane (1–2%), and a craniotomy (~ 1 mm diameter) was made above the GPe (AP -0.4 mm, ML 2.13 mm) or SNr (AP -3.16 mm, ML 1.30 mm). After dura removal, the craniotomy was covered with silicone elastomer (Kwik-Cast, WPI, Sarasota, FL, USA). Mice were allowed to recover in their home cage for at least 12 hours before recordings commenced. Recordings were made using optotrodes (ASSY-37-32-1-6mm or ASSY-37-32-1-9mm, Diagnostic Biochips, Glen Burnie, MD, USA). For electrophysiological recordings, we included only sessions in which PV or FoxP2 neurons were identified and found to be task-modulated. Among these, the stimulus contrast was 100% in most sessions (n = 50) and 15% in a subset of sessions (n = 24). Following recording, the electrode was retracted, the craniotomy was cleaned with saline, and covered with silicone elastomer. Each mouse underwent 1 – 6 recording sessions. The electrodes were coated with fluorescent dye (DiO or DiI, Invitrogen, Eugene, OR, USA) to visualize the electrode tracks.

We used a Cerebus 64-channel or 32-channel system (Blackrock Microsystems, Salt Lake City, UT, USA) to amplify and filter neural signals. The signals were band-pass filtered between 250 and 7500 Hz, and the waveforms of spikes were detected by thresholding at 4 standard deviations above background noise. Spiking signals were sampled at 30 kHz. Offline spike sorting was performed using Offline Sorter V3 (Plexon Inc., Dallas, TX, USA) based on cluster analysis of principal component. Spike clusters were classified as single units if the interspike interval exceeded 1 ms and the p-value for multivariate analysis of variance tests on the clusters was less than 0.05.

Histology

The mice were deeply anesthetized with isoflurane and were perfused with 20 mL of saline followed by 20 mL of 4% paraformaldehyde (PFA). The brains were removed and postfixed in 4% PFA overnight at 4°C. After fixation, the brains were transferred to 30% sucrose in phosphate-buffered saline (PBS) for 2 days at 4°C. The brains were sectioned into 60- or 40-μm coronal slices using a cryostat (NX50, Thermo Fisher Scientific, Waltham, MA, USA). To visualize EYFP fluorescence for brain sections from mice in which AAV2/5-EF1α-DIO-eNpHR3.0-EYFP-WPRE-hGH pA or AAV5-EF1α-DIO-eNpHR3.0-EYFP was injected in the GPe, slices were incubated in blocking solution (20% BSA, 0.5% Triton X-100 in PBS) for 2 h at room temperature, followed by incubation with primary antibodies (rabbit anti-GFP, 1:800, Invitrogen, G10362) overnight at 4°C. After rinsing with PBS, sections were incubated with secondary antibodies (donkey anti-rabbit Alexa Fluor or goat anti-rabbit Alexa Fluor, 1:1000,

Invitrogen, A21206 or A21245) for 2 h at room temperature. The sections were then washed in PBS and mounted using DAPI Fluoromount-G (SouthernBiotech, 0100-20, Birmingham, AL, USA); DAPI solution (Solarbio, C0065, Beijing, China) was included in a subset of sections. Fluorescence images were acquired using VS120 (Olympus, Tokyo, Japan). Selected slices were also imaged using a confocal microscope (FV3000, Olympus, Tokyo, Japan). Images were analyzed with ImageJ (NIH, Bethesda, MD, USA).

QUANTIFICATION AND STATISTICAL ANALYSIS

Data analysis

Analyses were performed using MATLAB (MathWorks Inc., Natick, MA, USA) or GraphPad Prism (GraphPad Software Inc., San Diego, CA, USA).

Behavioral performance was quantified as follows:

Hit rate = number of Hit trials/(number of Hit trials + number of Miss trials),

FA rate = number of FA trials/(number of FA trials + number of CR trials),

Behavioral discriminability (d′) = norminv(Hit rate) - norminv(FA rate), where norminv is the inverse of the cumulative normal function.

For optogenetic experiments, changes in behavioral performance (ΔHit rate, ΔFA rate, or Δd′) were calculated as the difference between the metric in laser-on and laser-off trials.

To determine whether a neuron was task-modulated, we performed a three-way ANOVA with the following factors: stimulus (Go versus No-Go), action (lick versus no

lick), and epoch that contained three periods (a 2-s period during inter-trial interval, the 0.5-s of waiting period, and the first 2-s of answer period). A neuron was considered task-modulated if any main effect or interaction term reached significance ($p < 0.01$) and was included in the analysis. Only task-modulated neurons with mean firing rate > 1 Hz were included in subsequent analyses.

We identified putative GABAergic SNr neurons based on their spike waveforms.[49] We computed the peak width, defined as the width at half-maximum of the waveform peak amplitude. Neurons with a peak width less than 0.36 ms were classified as GABAergic SNr neurons.[42] Only units with baseline firing rates exceeding 5 Hz during the first 10 s of the session were used in subsequent analyses.

We used a generalized linear model (GLM)[46] to quantify the task-related activity of GPe or SNr neurons. Spike counts from each session were binned into 100 ms intervals and Z-scored. The neuronal response at time t was modeled as a linear combination of multiple task events at various temporal delays relative to event onset:

$$R(t) = \beta_0 + \sum_{n=-2}^{5} \beta_n^{G} F_{t-n}^{G} + \sum_{n=-2}^{5} \beta_n^{NG} F_{t-n}^{NG} + \sum_{n=-6}^{29} \beta_n^{L_{on}} F_{t-n}^{L_{on}} + \sum_{n=-6}^{79} \beta_n^{L_{off}} F_{t-n}^{L_{off}} + \sum_{n=-2}^{47} \beta_n^{Hit} F_{t-n}^{Hit} + \sum_{n=-25}^{4} \beta_n^{CR} F_{t-n}^{CR} + \sum_{n=-2}^{47} \beta_n^{FA} F_{t-n}^{FA} ,$$

where β_0 is the offset term, β_n^x denotes the coefficient for task event x at temporal delay n, and F_t^x indicates the occurrence of event x at time bin t (1 if occurred, 0 otherwise). Here, G and NG represent the Go and No-Go stimuli, respectively; L_{on} and L_{off} denote lick-bout onset and offset; and Hit, CR, and FA correspond to reward, correct rejection, and false alarm events, respectively. Lick-bout onset was defined as a lick preceded by at least 2 s without licks; lick-bout offset as the last lick in a bout not

followed by another lick within 2 s. The time zero of Hit events was defined as the time of first lick following reward delivery in Go trial, whereas for FA events, it was defined as the time of sound cue triggered by the first lick in the answer period of No-Go trials. The time zero of CR events was defined as the end of answer period, with the analysis focused on neural dynamics related to the decision to withhold licking. Miss trials were not modeled as a separate regressor due to their low occurrence. The model had a total of 268 coefficients plus the offset term. For GPe neurons, only those with more than 10 trials for each event type were included in the GLM analysis. For SNr neurons, only those with more than 5 trials per event type in both laser-off and laser-on conditions were included.

The GLM models were fit using ridge regression.[46,77,78] We set aside 20% of trials as the test dataset. The remaining 80% of trials, used for model fitting, were further split into a training dataset (80%) and a validation dataset (20%). For each neuron, a regularization parameter λ was selected from a range of candidate values by maximizing model performance on the validation dataset. Model performance was quantified by the correlation coefficient (CC) between predicted and measured neural activity in the validation dataset. This cross-validation procedure was repeated 10 times, and the λ value that yielded the highest average CC on the validation sets was chosen. Using this optimal λ, the model was then fit on the combined training and validation data. Final model performance was assessed by computing the CC between the predicted and observed responses in the held-out test dataset. To estimate statistical significance, we bootstrapped the test dataset 1000 times to obtain a distribution of CC

values, and calculated a p-value as the proportion of CC ≤ 0. Neurons were considered to have significant GLM fits if the observed CC was positive and exceeded chance level ($p < 0.05$, bootstrap test), and were subsequently included in analysis.

The mean GLM coefficient for each regressor was computed over specified time windows (Go or No-Go stimulus: 0 – 0.5 s; lick-bout onset: 0 – 1.5 s; lick-bout offset: 0 – 1.5 s; Hit: 0 – 1 s; CR: -1 – 0 s, with time zero defined as the end of answer period; FA: 0 – 1 s).

Cue SI was computed as $(\beta_{Go} - \beta_{No\text{-}Go})/(|\beta_{Go}| + |\beta_{No\text{-}Go}|)$, in which β_{Go} and $\beta_{No\text{-}Go}$ represent the average GLM coefficients in the 0 – 0.5 s window after stimulus onset in Go and No-Go trials, respectively. For the sliding-window analysis of the cue SI at each time point, the denominator was fixed as the sum of the mean absolute β_{Go} and the mean absolute $\beta_{No\text{-}Go}$ values computed across all time points. The cue SI ranged from -1 to 1, with negative and positive values indicating preference for No-Go and Go stimuli, respectively. Outcome SI was calculated as $(\beta_{Hit} - \beta_{FA})/(|\beta_{Hit}| + |\beta_{FA}|)$, where β_{Hit} and β_{FA} represent the average coefficients in the 0 – 1 s window in Hit and FA trials, respectively. For the sliding-window analysis of the outcome SI at each time point, the denominator was fixed as the sum of the mean absolute β_{Hit} and the mean absolute β_{FA} values computed across all time points. The outcome SI ranged from -1 to 1, with negative values indicating a preference for FA outcome and positive values indicating a preference for Hit outcome.

We used a previously reported automated method[48] (AMaSiNe; https://github.com/vsnnlab/AMaSiNe) for quantification and three-dimensional (3D)

reconstruction of inputs to GPe neurons. This approach automatically calibrates the 3D alignment angles of each brain slice to match the standardized 3D Allen Mouse Brain Atlas (https://mouse.brain-map.org) and assigns the position of each neuron within the atlas. Only mice with more than 70% of starter cells confined to the GPe were included in the analysis. Based on this criterion, 4 of 13 PV-Cre mice and 3 of 12 FoxP2-Cre mice were retained. In the included animals, PV-Cre mice had 316.50 ± 57.71 (mean ± SEM) starter cells in the GPe, whereas FoxP2-Cre mice had 29.33 ± 5.17 (mean ± SEM) starter cells in the GPe. Because 2 of the 3 FoxP2-Cre mice showed input neurons exclusively in the striatum, with virtually no detectable inputs in other brain regions, full-brain input analysis was performed only for PV neurons. For PV-Cre mice, the number of detected neurons in each brain region was normalized to the total number of detected neurons across the entire brain, excluding neurons in the GPe. Only regions with an input percentage above 0.5% were analyzed.

To determine whether inactivation of GPe PV neurons significantly affects the firing rates of SNr neurons, we performed a two-way ANOVA on PSTHs (0 – 3 s relative to stimulus onset, 100 ms/bin). Comparisons were made between laser-off and laser-on conditions for both Go and No-Go trials. An SNr neuron was considered significantly affected if the p-value in either Go or No-Go condition was < 0.01. The mean firing rate for each SNr neuron was computed based on spikes within 0 – 3 s relative to stimulus onset.

REFERENCES

1. Gittis, A.H., Berke, J.D., Bevan, M.D., Chan, C.S., Mallet, N., Morrow, M.M., and Schmidt, R. (2014). New roles for the external globus pallidus in basal ganglia circuits and behavior. J Neurosci *34*, 15178-15183. 10.1523/JNEUROSCI.3252-14.2014.
2. Hegeman, D.J., Hong, E.S., Hernandez, V.M., and Chan, C.S. (2016). The external globus pallidus: progress and perspectives. Eur J Neurosci *43*, 1239-1265. 10.1111/ejn.13196.
3. Dong, J., Hawes, S., Wu, J., Le, W., and Cai, H. (2021). Connectivity and functionality of the globus pallidus externa under normal conditions and Parkinson's disease. Front Neural Circuits *15*, 645287. 10.3389/fncir.2021.645287.
4. Giossi, C., Rubin, J.E., Gittis, A., Verstynen, T., and Vich, C. (2024). Rethinking the external globus pallidus and information flow in cortico-basal ganglia-thalamic circuits. Eur J Neurosci. 10.1111/ejn.16348.
5. Courtney, C.D., Pamukcu, A., and Chan, C.S. (2023). Cell and circuit complexity of the external globus pallidus. Nat Neurosci *26*, 1147-1159. 10.1038/s41593-023-01368-7.
6. Courtney, C.D., and Chan, C.S. (2023). Cell type-specific processing of non-motor signals in the external pallidum. Trends Neurosci *46*, 336-337. 10.1016/j.tins.2023.03.002.
7. Nambu, A., and Chiken, S. (2024). External segment of the globus pallidus in health and disease: Its interactions with the striatum and subthalamic nucleus. Neurobiol Dis *190*, 106362. 10.1016/j.nbd.2023.106362.
8. Gerfen, C.R., Engber, T.M., Mahan, L.C., Susel, Z., Chase, T.N., Monsma, F.J., Jr., and Sibley, D.R. (1990). D1 and D2 dopamine receptor-regulated gene expression of striatonigral and striatopallidal neurons. Science *250*, 1429-1432.
9. Kita, H. (2007). Globus pallidus external segment. Prog Brain Res *160*, 111-133. 10.1016/S0079-6123(06)60007-1.
10. Mastro, K.J., Bouchard, R.S., Holt, H.A., and Gittis, A.H. (2014). Transgenic mouse lines subdivide external segment of the globus pallidus (GPe) neurons and reveal distinct GPe output pathways. J Neurosci *34*, 2087-2099. 10.1523/JNEUROSCI.4646-13.2014.
11. Fang, L.Z., and Creed, M.C. (2024). Updating the striatal-pallidal wiring diagram. Nat Neurosci *27*, 15-27. 10.1038/s41593-023-01518-x.
12. Guilhemsang, L., and Mallet, N.P. (2024). Arkypallidal neurons in basal ganglia circuits: Unveiling novel pallidostriatal loops? Curr Opin Neurobiol *84*, 102814. 10.1016/j.conb.2023.102814.
13. Mallet, N., Micklem, B.R., Henny, P., Brown, M.T., Williams, C., Bolam, J.P., Nakamura, K.C., and Magill, P.J. (2012). Dichotomous organization of the external globus pallidus. Neuron *74*, 1075-1086. 10.1016/j.neuron.2012.04.027.
14. Abdi, A., Mallet, N., Mohamed, F.Y., Sharott, A., Dodson, P.D., Nakamura, K.C., Suri, S., Avery, S.V., Larvin, J.T., Garas, F.N., et al. (2015). Prototypic and arkypallidal neurons in the dopamine-intact external globus pallidus. J Neurosci *35*, 6667-6688. 10.1523/JNEUROSCI.4662-14.2015.

15. Dodson, P.D., Larvin, J.T., Duffell, J.M., Garas, F.N., Doig, N.M., Kessaris, N., Duguid, I.C., Bogacz, R., Butt, S.J., and Magill, P.J. (2015). Distinct developmental origins manifest in the specialized encoding of movement by adult neurons of the external globus pallidus. Neuron *86*, 501-513. 10.1016/j.neuron.2015.03.007.
16. Hernandez, V.M., Hegeman, D.J., Cui, Q., Kelver, D.A., Fiske, M.P., Glajch, K.E., Pitt, J.E., Huang, T.Y., Justice, N.J., and Chan, C.S. (2015). Parvalbumin+ neurons and Npas1+ neurons are distinct neuron classes in the mouse external globus pallidus. J Neurosci *35*, 11830-11847. 10.1523/JNEUROSCI.4672-14.2015.
17. Saunders, A., Huang, K.W., and Sabatini, B.L. (2016). Globus pallidus externus neurons expressing parvalbumin interconnect the subthalamic nucleus and striatal interneurons. PLoS One *11*, e0149798. 10.1371/journal.pone.0149798.
18. Cui, Q., Pamukcu, A., Cherian, S., Chang, I.Y.M., Berceau, B.L., Xenias, H.S., Higgs, M.H., Rajamanickam, S., Chen, Y., Du, X., et al. (2021). Dissociable roles of pallidal neuron subtypes in regulating motor patterns. J Neurosci *41*, 4036-4059. 10.1523/JNEUROSCI.2210-20.2021.
19. Abecassis, Z.A., Berceau, B.L., Win, P.H., Garcia, D., Xenias, H.S., Cui, Q., Pamukcu, A., Cherian, S., Hernandez, V.M., Chon, U., et al. (2020). Npas1(+)-Nkx2.1(+) neurons are an integral part of the cortico-pallido-cortical loop. J Neurosci *40*, 743-768. 10.1523/JNEUROSCI.1199-19.2019.
20. Pamukcu, A., Cui, Q., Xenias, H.S., Berceau, B.L., Augustine, E.C., Fan, I., Chalasani, S., Hantman, A.W., Lerner, T.N., Boca, S.M., and Chan, C.S. (2020). Parvalbumin(+) and Npas1(+) pallidal neurons have distinct circuit topology and function. J Neurosci *40*, 7855-7876. 10.1523/JNEUROSCI.0361-20.2020.
21. Mallet, N., Schmidt, R., Leventhal, D., Chen, F., Amer, N., Boraud, T., and Berke, J.D. (2016). Arkypallidal cells send a stop signal to striatum. Neuron *89*, 308-316. 10.1016/j.neuron.2015.12.017.
22. Lilascharoen, V., Wang, E.H., Do, N., Pate, S.C., Tran, A.N., Yoon, C.D., Choi, J.H., Wang, X.Y., Pribiag, H., Park, Y.G., et al. (2021). Divergent pallidal pathways underlying distinct Parkinsonian behavioral deficits. Nat Neurosci *24*, 504-515. 10.1038/s41593-021-00810-y.
23. Glajch, K.E., Kelver, D.A., Hegeman, D.J., Cui, Q., Xenias, H.S., Augustine, E.C., Hernandez, V.M., Verma, N., Huang, T.Y., Luo, M., et al. (2016). Npas1+ Pallidal Neurons Target Striatal Projection Neurons. J Neurosci *36*, 5472-5488. 10.1523/JNEUROSCI.1720-15.2016.
24. Aristieta, A., Barresi, M., Azizpour Lindi, S., Barriere, G., Courtand, G., de la Crompe, B., Guilhemsang, L., Gauthier, S., Fioramonti, S., Baufreton, J., and Mallet, N.P. (2021). A disynaptic circuit in the globus pallidus controls locomotion inhibition. Curr Biol *31*, 707-721 e707. 10.1016/j.cub.2020.11.019.
25. Labouesse, M.A., Torres-Herraez, A., Chohan, M.O., Villarin, J.M., Greenwald, J., Sun, X., Zahran, M., Tang, A., Lam, S., Veenstra-VanderWeele, J., et al. (2023). A non-canonical striatopallidal Go pathway that supports motor control. Nat Commun *14*, 6712. 10.1038/s41467-023-42288-1.

26. Mastro, K.J., Zitelli, K.T., Willard, A.M., Leblanc, K.H., Kravitz, A.V., and Gittis, A.H. (2017). Cell-specific pallidal intervention induces long-lasting motor recovery in dopamine-depleted mice. Nat Neurosci *20*, 815-823. 10.1038/nn.4559.
27. Spix, T.A., Nanivadekar, S., Toong, N., Kaplow, I.M., Isett, B.R., Goksen, Y., Pfenning, A.R., and Gittis, A.H. (2021). Population-specific neuromodulation prolongs therapeutic benefits of deep brain stimulation. Science *374*, 201-206. 10.1126/science.abi7852.
28. Shen, C., Shen, B., Liu, D., Han, L., Zou, K., Gan, L., Ren, J., Wu, B., Tang, Y., Zhao, J., et al. (2024). Bidirectional regulation of levodopa-induced dyskinesia by a specific neural ensemble in globus pallidus external segment. Cell Rep Med *5*, 101566. 10.1016/j.xcrm.2024.101566.
29. Xu, Z., Duan, W., Yuan, S., Zhang, X., You, C., Yu, J.T., Wang, J., Li, J.D., Deng, S., and Shu, Y. (2025). Deep brain stimulation alleviates Parkinsonian motor deficits through desynchronizing GABA release in mice. Nat Commun *16*, 3726. 10.1038/s41467-025-59113-6.
30. Schechtman, E., Noblejas, M.I., Mizrahi, A.D., Dauber, O., and Bergman, H. (2016). Pallidal spiking activity reflects learning dynamics and predicts performance. Proc Natl Acad Sci U S A *113*, E6281-E6289. 10.1073/pnas.1612392113.
31. Kim, H.F., Amita, H., and Hikosaka, O. (2017). Indirect Pathway of Caudal Basal Ganglia for Rejection of Valueless Visual Objects. Neuron *94*, 920-930 e923. 10.1016/j.neuron.2017.04.033.
32. Arkadir, D., Morris, G., Vaadia, E., and Bergman, H. (2004). Independent coding of movement direction and reward prediction by single pallidal neurons. J Neurosci *24*, 10047-10056. 10.1523/JNEUROSCI.2583-04.2004.
33. Katabi, S., Adler, A., Deffains, M., and Bergman, H. (2023). Dichotomous activity and function of neurons with low- and high-frequency discharge in the external globus pallidus of non-human primates. Cell Rep *42*, 111898. 10.1016/j.celrep.2022.111898.
34. Farries, M.A., Faust, T.W., Mohebi, A., and Berke, J.D. (2023). Selective encoding of reward predictions and prediction errors by globus pallidus subpopulations. Curr Biol *33*, 4124-4135 e4125. 10.1016/j.cub.2023.08.042.
35. Baker, M., Kang, S., Hong, S.I., Song, M., Yang, M.A., Peyton, L., Essa, H., Lee, S.W., and Choi, D.S. (2023). External globus pallidus input to the dorsal striatum regulates habitual seeking behavior in male mice. Nat Commun *14*, 4085. 10.1038/s41467-023-39545-8.
36. Isett, B.R., Nguyen, K.P., Schwenk, J.C., Yurek, J.R., Snyder, C.N., Vounatsos, M.V., Adegbesan, K.A., Ziausyte, U., and Gittis, A.H. (2023). The indirect pathway of the basal ganglia promotes transient punishment but not motor suppression. Neuron *111*, 2218-2231 e2214. 10.1016/j.neuron.2023.04.017.
37. Tian, G., Bartas, K., Hui, M., Chen, L., Vasquez, J.J., Azouz, G., Derdeyn, P., Manville, R.W., Ho, E.L., Fang, A.S., et al. (2024). Molecular and circuit determinants in the globus pallidus mediating control of cocaine-induced

behavioral plasticity. Neuron. 10.1016/j.neuron.2024.07.018.
38. Beier, K.T., Kim, C.K., Hoerbelt, P., Hung, L.W., Heifets, B.D., DeLoach, K.E., Mosca, T.J., Neuner, S., Deisseroth, K., Luo, L., and Malenka, R.C. (2017). Rabies screen reveals GPe control of cocaine-triggered plasticity. Nature *549*, 345-350. 10.1038/nature23888.
39. Ketzef, M., and Silberberg, G. (2021). Differential synaptic input to external globus pallidus neuronal subpopulations in vivo. Neuron *109*, 516-529 e514. 10.1016/j.neuron.2020.11.006.
40. Johansson, Y., and Ketzef, M. (2023). Sensory processing in external globus pallidus neurons. Cell Rep *42*, 111952. 10.1016/j.celrep.2022.111952.
41. Liu, J., Liu, D., Pu, X., Zou, K., Xie, T., Li, Y., and Yao, H. (2023). The secondary motor cortex-striatum circuit contributes to suppressing inappropriate responses in perceptual decision behavior. Neurosci Bull *39*, 1544-1560. 10.1007/s12264-023-01073-2.
42. Chen, Z., Zhang, Z.Y., Zhang, W., Xie, T., Li, Y., Xu, X.H., and Yao, H. (2021). Direct and indirect pathway neurons in ventrolateral striatum differentially regulate licking movement and nigral responses. Cell Rep *37*, 109847. 10.1016/j.celrep.2021.109847.
43. Lee, K., Bakhurin, K.I., Claar, L.D., Holley, S.M., Chong, N.C., Cepeda, C., Levine, M.S., and Masmanidis, S.C. (2019). Gain modulation by corticostriatal and thalamostriatal input signals during reward-conditioned behavior. Cell Rep *29*, 2438-2449 e2434. 10.1016/j.celrep.2019.10.060.
44. Alcaraz, F., Marchand, A.R., Courtand, G., Coutureau, E., and Wolff, M. (2016). Parallel inputs from the mediodorsal thalamus to the prefrontal cortex in the rat. Eur J Neurosci *44*, 1972-1986. 10.1111/ejn.13316.
45. Koene, L.M.C., Thunberg, W., Grillner, S., Silberberg, G., and Ketzef, M. (2025). Cellular and synaptic properties of molecularly defined neurons in the external globus pallidus. iScience *28*, 113002. 10.1016/j.isci.2025.113002.
46. Pinto, L., and Dan, Y. (2015). Cell-type-specific activity in prefrontal cortex during goal-directed behavior. Neuron *87*, 437-450. 10.1016/j.neuron.2015.06.021.
47. Li, Y., Lopez-Huerta, V.G., Adiconis, X., Levandowski, K., Choi, S., Simmons, S.K., Arias-Garcia, M.A., Guo, B., Yao, A.Y., Blosser, T.R., et al. (2020). Distinct subnetworks of the thalamic reticular nucleus. Nature *583*, 819-824. 10.1038/s41586-020-2504-5.
48. Song, J.H., Choi, W., Song, Y.H., Kim, J.H., Jeong, D., Lee, S.H., and Paik, S.B. (2020). Precise mapping of single neurons by calibrated 3D reconstruction of brain slices reveals topographic projection in mouse visual cortex. Cell Rep *31*, 107682. 10.1016/j.celrep.2020.107682.
49. Barter, J.W., Li, S., Sukharnikova, T., Rossi, M.A., Bartholomew, R.A., and Yin, H.H. (2015). Basal ganglia outputs map instantaneous position coordinates during behavior. J Neurosci *35*, 2703-2716. 10.1523/JNEUROSCI.3245-14.2015.
50. Karube, F., Takahashi, S., Kobayashi, K., and Fujiyama, F. (2019). Motor cortex

can directly drive the globus pallidus neurons in a projection neuron type-dependent manner in the rat. Elife *8*, e49511. 10.7554/eLife.49511.
51. Lee, J., Wang, W., and Sabatini, B.L. (2020). Anatomically segregated basal ganglia pathways allow parallel behavioral modulation. Nat Neurosci *23*, 1388-1398. 10.1038/s41593-020-00712-5.
52. Foster, N.N., Barry, J., Korobkova, L., Garcia, L., Gao, L., Becerra, M., Sherafat, Y., Peng, B., Li, X., Choi, J.H., et al. (2021). The mouse cortico-basal ganglia-thalamic network. Nature *598*, 188-194. 10.1038/s41586-021-03993-3.
53. Wu, Y.W., and Ding, J.B. (2017). A cell-type-specific jolt for motor disorders. Nat Neurosci *20*, 763-765. 10.1038/nn.4565.
54. Yuan, X.S., Wang, L., Dong, H., Qu, W.M., Yang, S.R., Cherasse, Y., Lazarus, M., Schiffmann, S.N., d'Exaerde, A.K., Li, R.X., and Huang, Z.L. (2017). Striatal adenosine A(2A) receptor neurons control active-period sleep via parvalbumin neurons in external globus pallidus. Elife *6*, e29055. 10.7554/eLife.29055.
55. Peer, N.D., Yamin, H.G., and Cohen, D. (2022). Multidimensional encoding of movement and contextual variables by rat globus pallidus neurons during a novel environment exposure task. iScience *25*, 105024. 10.1016/j.isci.2022.105024.
56. Joshua, M., Adler, A., Rosin, B., Vaadia, E., and Bergman, H. (2009). Encoding of probabilistic rewarding and aversive events by pallidal and nigral neurons. J Neurophysiol *101*, 758-772. 10.1152/jn.90764.2008.
57. Nougaret, S., and Ravel, S. (2018). Dynamic Encoding of Effort and Reward throughout the Execution of Action by External Globus Pallidus Neurons in Monkeys. J Cogn Neurosci *30*, 1130-1144. 10.1162/jocn_a_01277.
58. Yoshida, A., and Hikosaka, O. (2025). Excitatory drive to the globus pallidus external segment facilitates action initiation in non-human primates. Curr Biol, S0960-9822(0925)00960-00961. 10.1016/j.cub.2025.07.051.
59. Hunt, A.J., Jr., Dasgupta, R., Rajamanickam, S., Jiang, Z., Beierlein, M., Chan, C.S., and Justice, N.J. (2018). Paraventricular hypothalamic and amygdalar CRF neurons synapse in the external globus pallidus. Brain Struct Funct *223*, 2685-2698. 10.1007/s00429-018-1652-y.
60. Chang, S., Fermani, F., Lao, C.L., Huang, L., Jakovcevski, M., Di Giaimo, R., Gagliardi, M., Menegaz, D., Hennrich, A.A., Ziller, M., et al. (2022). Tripartite extended amygdala-basal ganglia CRH circuit drives locomotor activation and avoidance behavior. Sci Adv *8*, eabo1023. 10.1126/sciadv.abo1023.
61. Ferenczi, E.A., Wang, W., Biswas, A., Pottala, T., Dong, Y., Chan, A.K., Albanese, M.A., Sohur, R.S., Jia, T., Mastro, K.J., and Sabatini, B.L. (2025). Reciprocal projections between the globus pallidus externa and cortex span motor and nonmotor regions. Proc Natl Acad Sci U S A *122*, e2423367122. 10.1073/pnas.2423367122.
62. Cui, Q., Du, X., Chang, I.Y.M., Pamukcu, A., Lilascharoen, V., Berceau, B.L., Garcia, D., Hong, D., Chon, U., Narayanan, A., et al. (2021). Striatal direct pathway targets Npas1(+) pallidal neurons. J Neurosci *41*, 3966-3987.

10.1523/JNEUROSCI.2306-20.2021.
63. Ma, M.F., Hu, J., Hao, Y.X., Zhang, K.Y., Zhang, X., Zhu, M.C., Zhou, Z.L., Yuan, X.S., and Yuan, F. (2025). Whole brain monosynaptic input of distinct neurons in the globus pallidus externa. CNS Neurosci Ther *31*, e70459. 10.1111/cns.70459.
64. Zatka-Haas, P., Steinmetz, N.A., Carandini, M., and Harris, K.D. (2021). Sensory coding and the causal impact of mouse cortex in a visual decision. Elife *10*, e63163. 10.7554/eLife.63163.
65. Mandelbaum, G., Taranda, J., Haynes, T.M., Hochbaum, D.R., Huang, K.W., Hyun, M., Umadevi Venkataraju, K., Straub, C., Wang, W., Robertson, K., et al. (2019). Distinct cortical-thalamic-striatal circuits through the parafascicular nucleus. Neuron *102*, 636-652 e637. 10.1016/j.neuron.2019.02.035.
66. Magno, L.A.V., Tenza-Ferrer, H., Collodetti, M., Aguiar, M.F.G., Rodrigues, A.P.C., da Silva, R.S., Silva, J.D.P., Nicolau, N.F., Rosa, D.V.F., Birbrair, A., et al. (2019). Optogenetic stimulation of the M2 cortex reverts motor dysfunction in a mouse model of Parkinson's disease. J Neurosci *39*, 3234-3248. 10.1523/JNEUROSCI.2277-18.2019.
67. Fan, D., Rossi, M.A., and Yin, H.H. (2012). Mechanisms of action selection and timing in substantia nigra neurons. J Neurosci *32*, 5534-5548. 10.1523/JNEUROSCI.5924-11.2012.
68. Aristieta, A., Parker, J.E., Gao, Y.E., Rubin, J.E., and Gittis, A.H. (2024). Dopamine depletion weakens direct pathway modulation of SNr neurons. Neurobiol Dis *196*, 106512. 10.1016/j.nbd.2024.106512.
69. Amita, H., and Hikosaka, O. (2019). Indirect pathway from caudate tail mediates rejection of bad objects in periphery. Sci Adv *5*, eaaw9297. 10.1126/sciadv.aaw9297.
70. Deniau, J.M., Mailly, P., Maurice, N., and Charpier, S. (2007). The pars reticulata of the substantia nigra: a window to basal ganglia output. Prog Brain Res *160*, 151-172. 10.1016/S0079-6123(06)60009-5.
71. Deniau, J.M., Kitai, S.T., Donoghue, J.P., and Grofova, I. (1982). Neuronal interactions in the substantia nigra pars reticulata through axon collaterals of the projection neurons. An electrophysiological and morphological study. Exp Brain Res *47*, 105-113. 10.1007/BF00235891.
72. Brown, J., Pan, W.X., and Dudman, J.T. (2014). The inhibitory microcircuit of the substantia nigra provides feedback gain control of the basal ganglia output. Elife *3*, e02397. 10.7554/eLife.02397.
73. Freeze, B.S., Kravitz, A.V., Hammack, N., Berke, J.D., and Kreitzer, A.C. (2013). Control of basal ganglia output by direct and indirect pathway projection neurons. J Neurosci *33*, 18531-18539. 10.1523/JNEUROSCI.1278-13.2013.
74. Hughes, R.N., Bakhurin, K.I., Barter, J.W., Zhang, J., and Yin, H.H. (2020). A head-fixation system for continuous monitoring of force generated during behavior. Front Integr Neurosci *14*, 11. 10.3389/fnint.2020.00011.
75. Qiu, L., Zhang, B., and Gao, Z. (2022). Lighting up neural circuits by viral

tracing. Neurosci Bull *38*, 1383-1396. 10.1007/s12264-022-00860-7.
76. Wall, N.R., Wickersham, I.R., Cetin, A., De La Parra, M., and Callaway, E.M. (2010). Monosynaptic circuit tracing in vivo through Cre-dependent targeting and complementation of modified rabies virus. Proc Natl Acad Sci U S A *107*, 21848-21853. 10.1073/pnas.1011756107.
77. Huth, A.G., Nishimoto, S., Vu, A.T., and Gallant, J.L. (2012). A continuous semantic space describes the representation of thousands of object and action categories across the human brain. Neuron *76*, 1210-1224. 10.1016/j.neuron.2012.10.014.
78. Pho, G.N., Goard, M.J., Woodson, J., Crawford, B., and Sur, M. (2018). Task-dependent representations of stimulus and choice in mouse parietal cortex. Nat Commun *9*, 2596. 10.1038/s41467-018-05012-y.

Figure 1

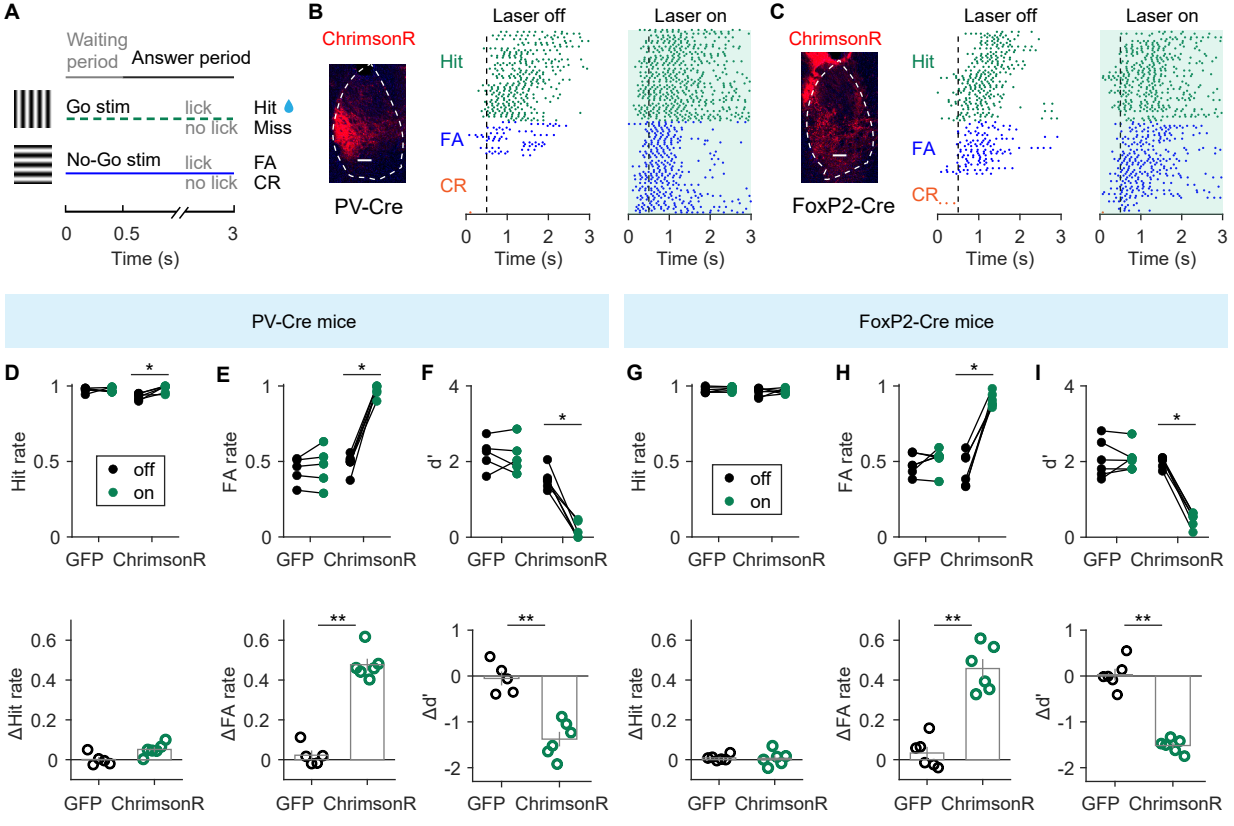
A
Waiting period
Answer period
Go stim
lick
no lick
Hit
Miss
No-Go stim
lick
no lick
FA
CR
0
0.5
3
Time (s)
B
ChrimsonR
PV-Cre
Laser off
Laser on
Hit
FA
CR
Time (s)
C
ChrimsonR
FoxP2-Cre
Laser off
Laser on
Hit
FA
CR
Time (s)
PV-Cre mice
FoxP2-Cre mice
D
E
F
G
H
I
Hit rate
FA rate
d'
off
on
GFP
ChrimsonR
ΔHit rate
ΔFA rate
Δd'
*
**

Figure 2

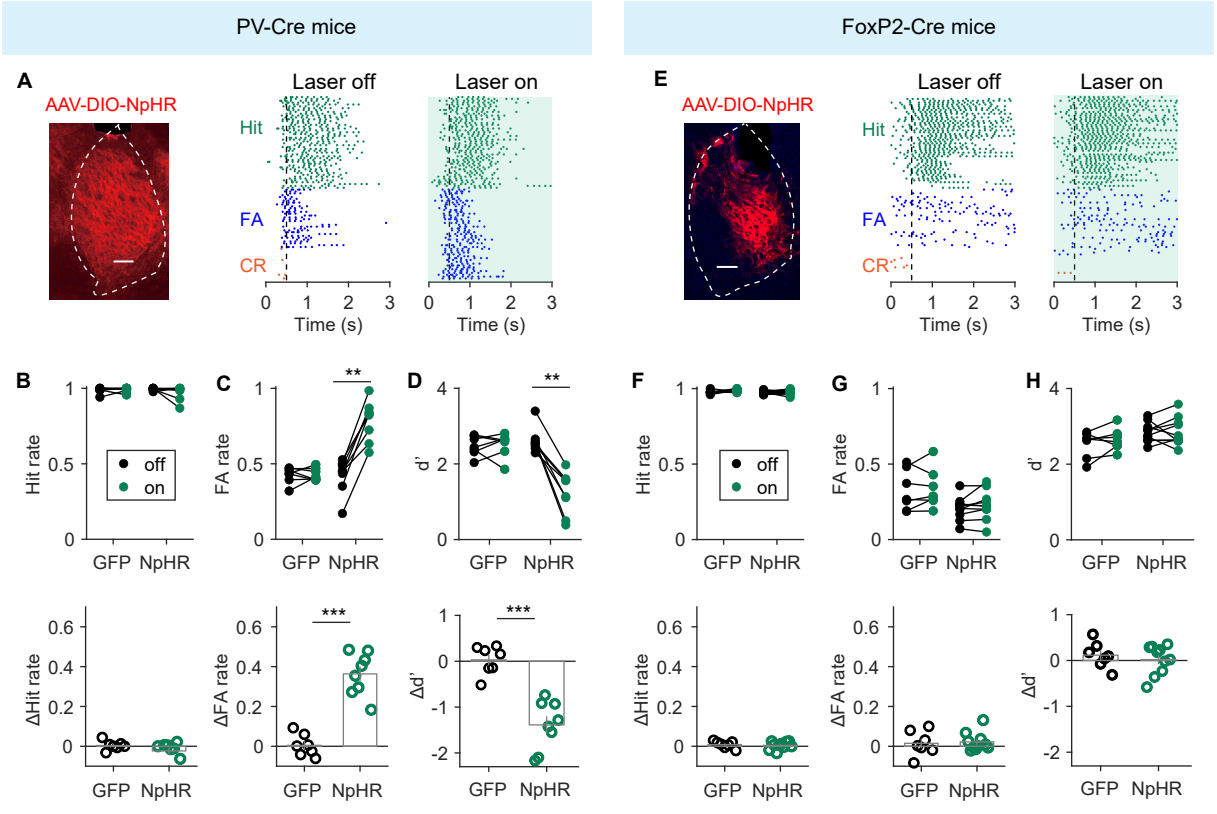
PV-Cre mice
FoxP2-Cre mice
A
AAV-DIO-NpHR
Laser off
Laser on
Hit
FA
CR
Time (s)
E
AAV-DIO-NpHR
Laser off
Laser on
Hit
FA
CR
Time (s)
B
Hit rate
off
on
GFP NpHR
C
FA rate
**
GFP NpHR
D
d'
**
GFP NpHR
F
Hit rate
off
on
GFP NpHR
G
FA rate
GFP NpHR
H
d'
GFP NpHR
ΔHit rate
GFP NpHR
ΔFA rate
***
GFP NpHR
Δd'
***
GFP NpHR
ΔHit rate
GFP NpHR
ΔFA rate
GFP NpHR
Δd'
GFP NpHR

Figure 3

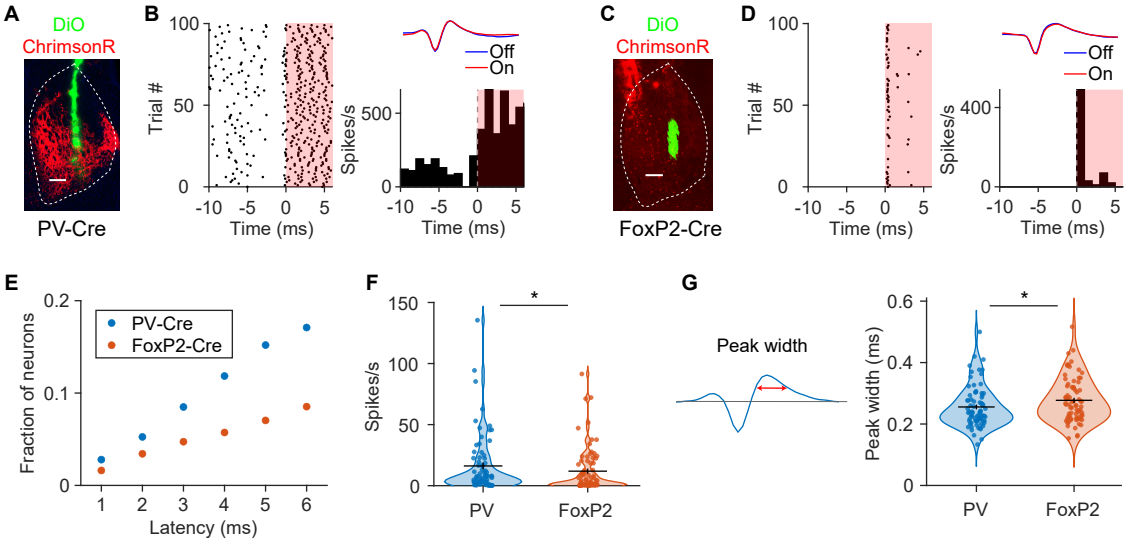
A
DiO
ChrimsonR
PV-Cre
B
Trial #
Time (ms)
Spikes/s
Off
On
C
DiO
ChrimsonR
FoxP2-Cre
D
Trial #
Time (ms)
Spikes/s
Off
On
E
Fraction of neurons
Latency (ms)
PV-Cre
FoxP2-Cre
F
Spikes/s
PV
FoxP2
G
Peak width
Peak width (ms)
PV
FoxP2

Figure 4

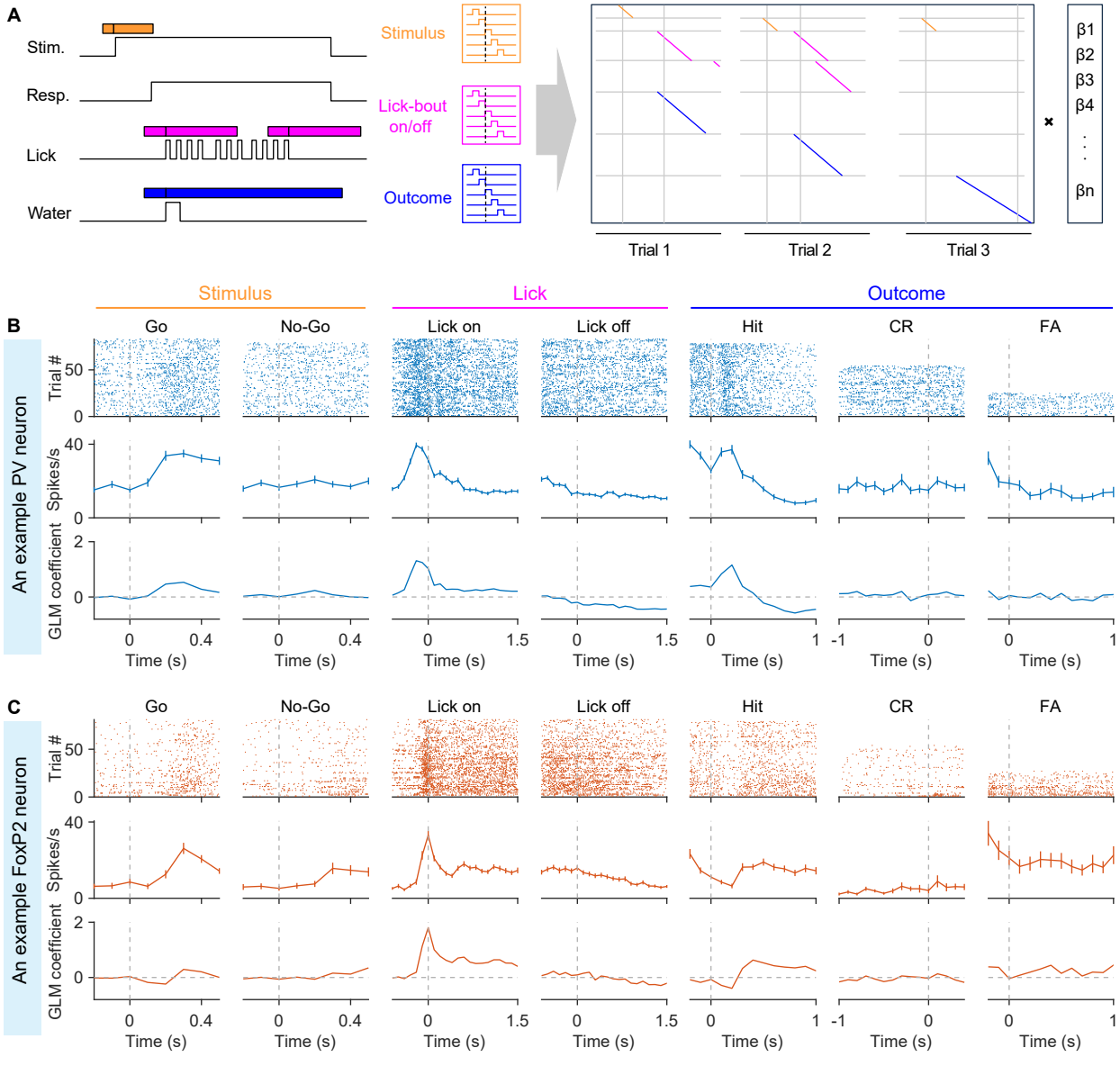
A
Stim.
Resp.
Lick
Water
Stimulus
Lick-bout on/off
Outcome
Trial 1
Trial 2
Trial 3
β1
β2
β3
β4
βn
B
Stimulus
Lick
Outcome
Go
No-Go
Lick on
Lick off
Hit
CR
FA
An example PV neuron
Trial #
Spikes/s
GLM coefficient
Time (s)
C
An example FoxP2 neuron

Figure 5

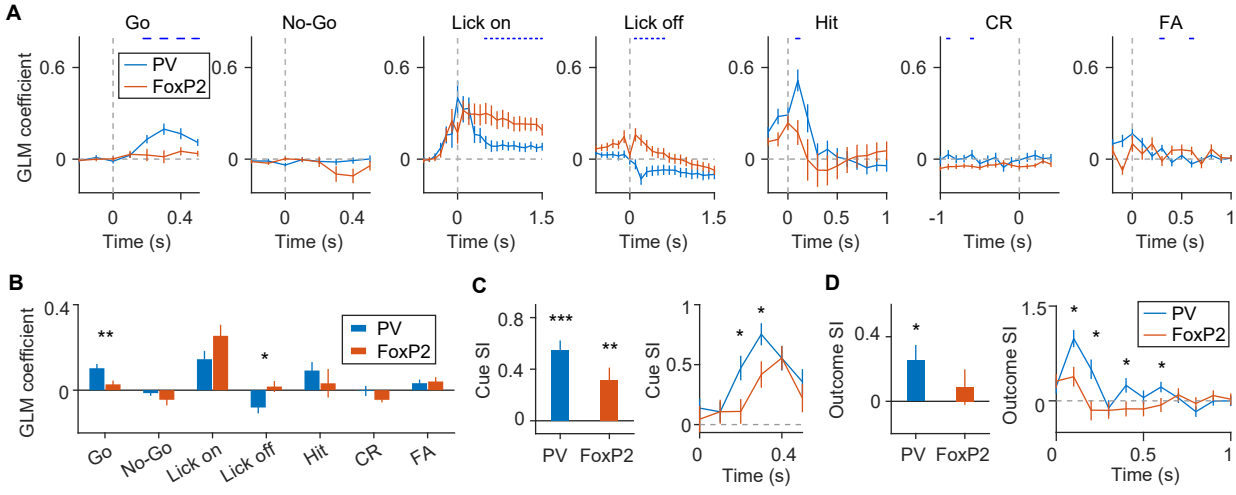
A
Go
No-Go
Lick on
Lick off
Hit
CR
FA
PV
FoxP2
GLM coefficient
Time (s)
B
GLM coefficient
PV
FoxP2
Go
No-Go
Lick on
Lick off
Hit
CR
FA
C
Cue SI
PV
FoxP2
Time (s)
D
Outcome SI
PV
FoxP2
Time (s)

Figure 6

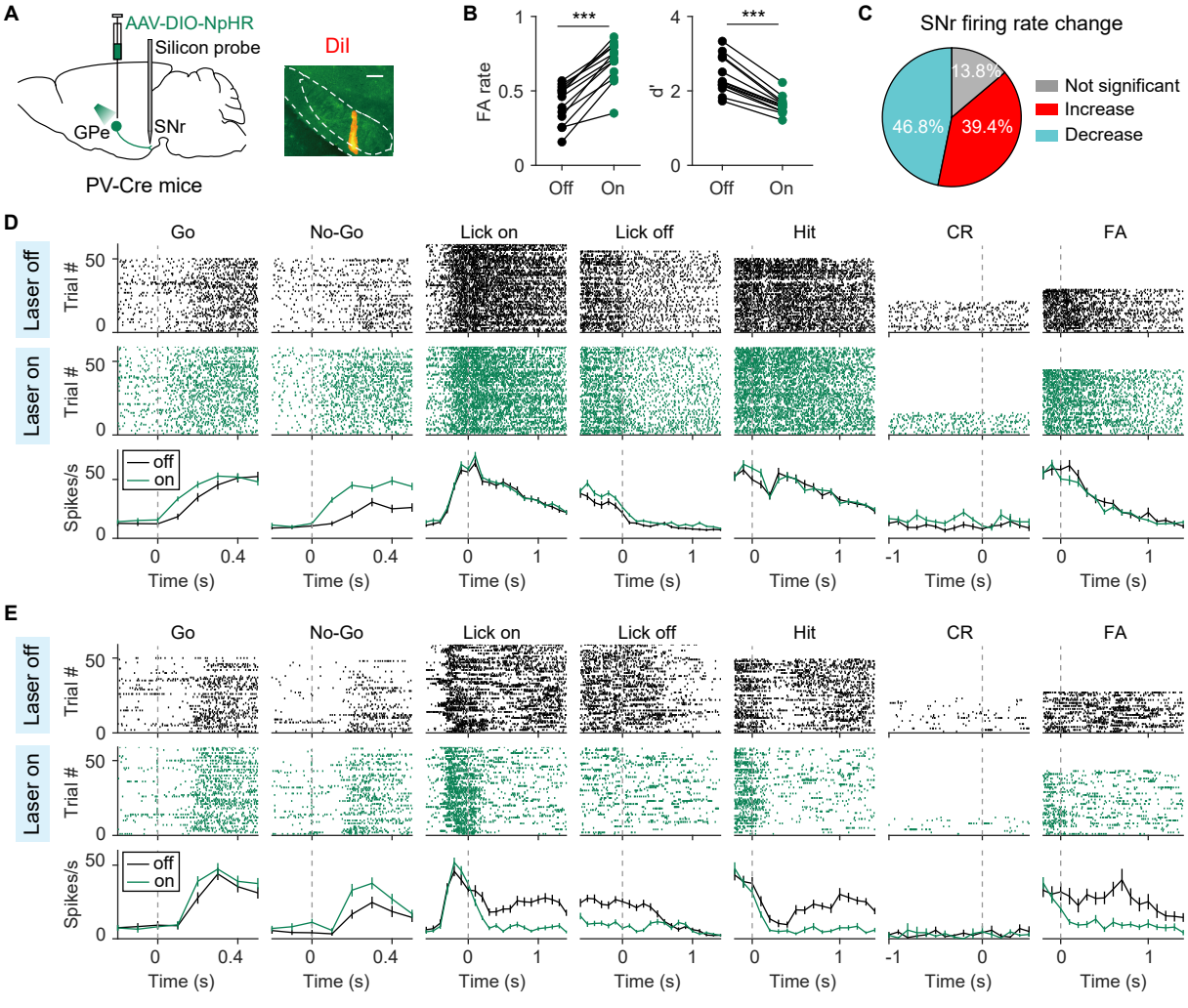
A
AAV-DIO-NpHR
Silicon probe
GPe
SNr
PV-Cre mice
DiI
B
FA rate
d'
***
Off
On
C
SNr firing rate change
13.8%
39.4%
46.8%
Not significant
Increase
Decrease
D
E
Go
No-Go
Lick on
Lick off
Hit
CR
FA
Laser off
Laser on
Trial #
Spikes/s
off
on
Time (s)

Figure 7

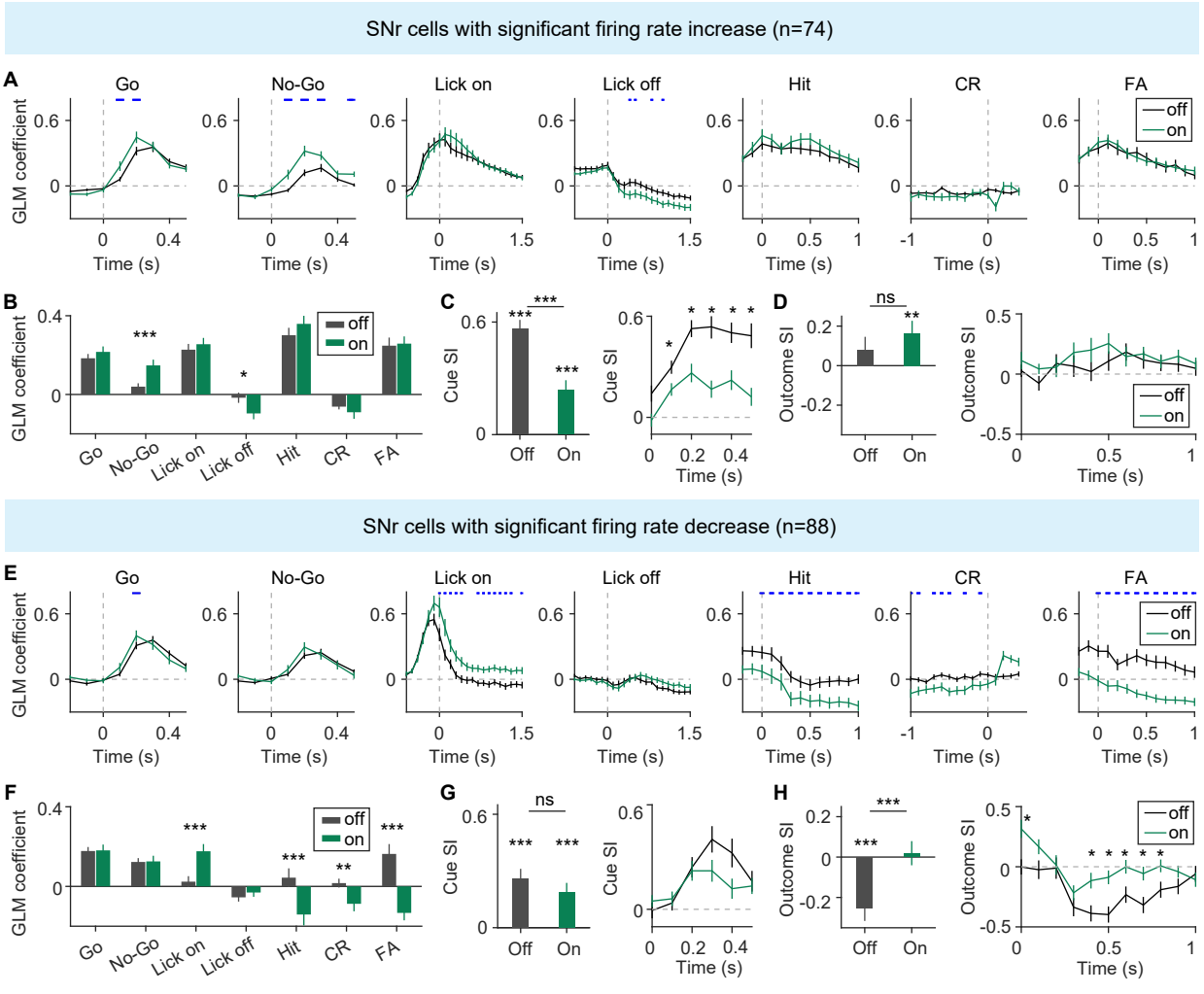
SNr cells with significant firing rate increase (n=74)
A
Go
No-Go
Lick on
Lick off
Hit
CR
FA
GLM coefficient
Time (s)
off
on
B
C
D
Cue SI
Outcome SI
Off
On
ns
SNr cells with significant firing rate decrease (n=88)
E
F
G
H

Distinct contributions and sensorimotor encoding of PV and FoxP2 neurons in the external globus pallidus during perceptual decision-making

Xiaotian Pu, Jingyu Ren, Taorong Xie, Kexin Zou, Jingze Xu, Yaping Li, Dechen Liu, and Haishan Yao

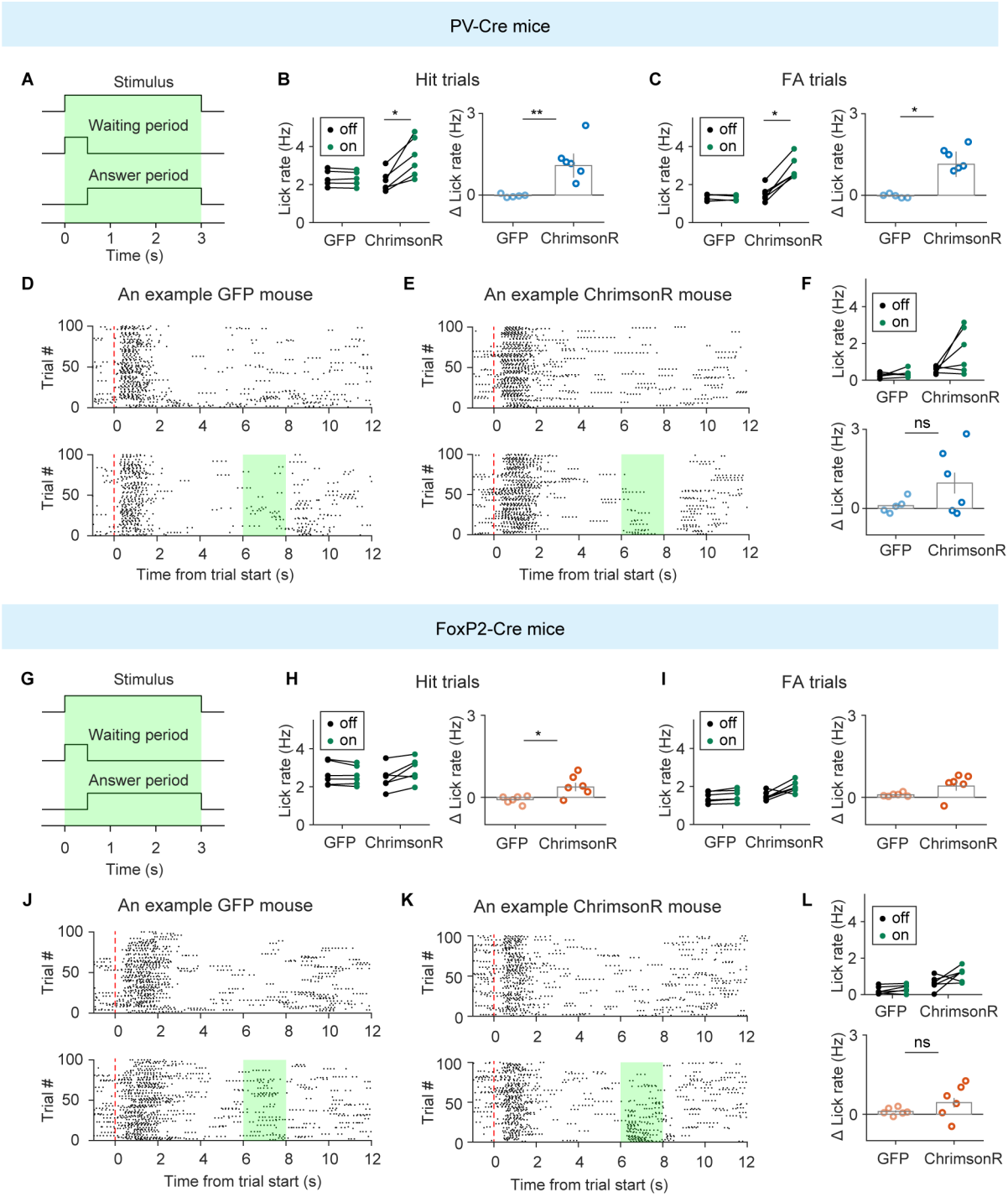

Figure S1. Effect of activating PV or FoxP2 GPe neurons on lick rate during stimulus period or inter-trial interval (ITI). Related to Figure 1.

(A) Schematic of the duration of laser stimulation (green shading) during stimulus presentation period.

(B) Left, lick rates during stimulus period in Hit trials under laser-off and laser-on conditions for PV-Cre mice expressing AAV-FLEX-EGFP (n = 5) or AAV-FLEX-ChrimsonR (n = 6) in the GPe. *p < 0.05, Wilcoxon signed-rank test. Right, comparison of lick rate difference between control and ChrimsonR mice. **p < 0.01, Wilcoxon rank-sum test.

(C) Same as (A), but for FA trials. Left, *p < 0.05, Wilcoxon signed-rank test. Right, *p < 0.05, Wilcoxon rank-sum test.

(D) Lick rasters from an example PV-Cre mouse expressing AAV-FLEX-EGFP in the GPe. Top, laser-off trials. Bottom, laser stimulation was applied during the ITI. Green shading, laser stimulation period.

(E) Same as (D), but for a PV-Cre mouse expressing AAV-FLEX-ChrimsonR in the GPe.

(F) Top, ITI lick rates under laser-off and laser-on conditions for GFP mice ($n = 5$, $p = 0.63$, Wilcoxon signed-rank test) and ChrimsonR PV-Cre mice ($n = 6$, $p = 0.16$, Wilcoxon signed-rank test). Bottom, comparison of ITI laser-induced lick rate changes between GFP and ChrimsonR PV-Cre mice ($p = 0.28$, Wilcoxon rank-sum test).

(G) Schematic of the duration of laser stimulation (green shading) during stimulus presentation period.

(H) Left, lick rates during stimulus period in Hit trials under laser-off and laser-on conditions for FoxP2-Cre mice expressing AAV-FLEX-EGFP ($n = 6$) or AAV-FLEX-ChrimsonR ($n = 6$) in the GPe. Right, comparison of lick rate difference between control and ChrimsonR mice. $^*p < 0.05$, Wilcoxon rank-sum test.

(I) Same as (G), but for FA trials.

(J) Lick rasters from an example FoxP2-Cre mouse expressing AAV-FLEX-EGFP in the GPe. Top, laser-off trials. Bottom, laser stimulation was applied during the ITI. Green shading, laser stimulation period.

(K) Same as (J), but for a FoxP2-Cre mouse expressing AAV-FLEX-ChrimsonR in the GPe.

(L) Top, ITI lick rates under laser-off and laser-on conditions for GFP mice ($n = 6$, $p = 0.22$, Wilcoxon signed-rank test) and ChrimsonR FoxP2-Cre mice ($n = 6$, $p = 0.16$, Wilcoxon signed-rank test). Bottom, comparison of ITI laser-induced lick rate changes between GFP and ChrimsonR FoxP2-Cre mice ($p = 0.19$, Wilcoxon rank-sum test).

For display purposes, 100 laser-off trials and 100 laser-on trials were shown in the raster plot. Data represent mean ± SEM.

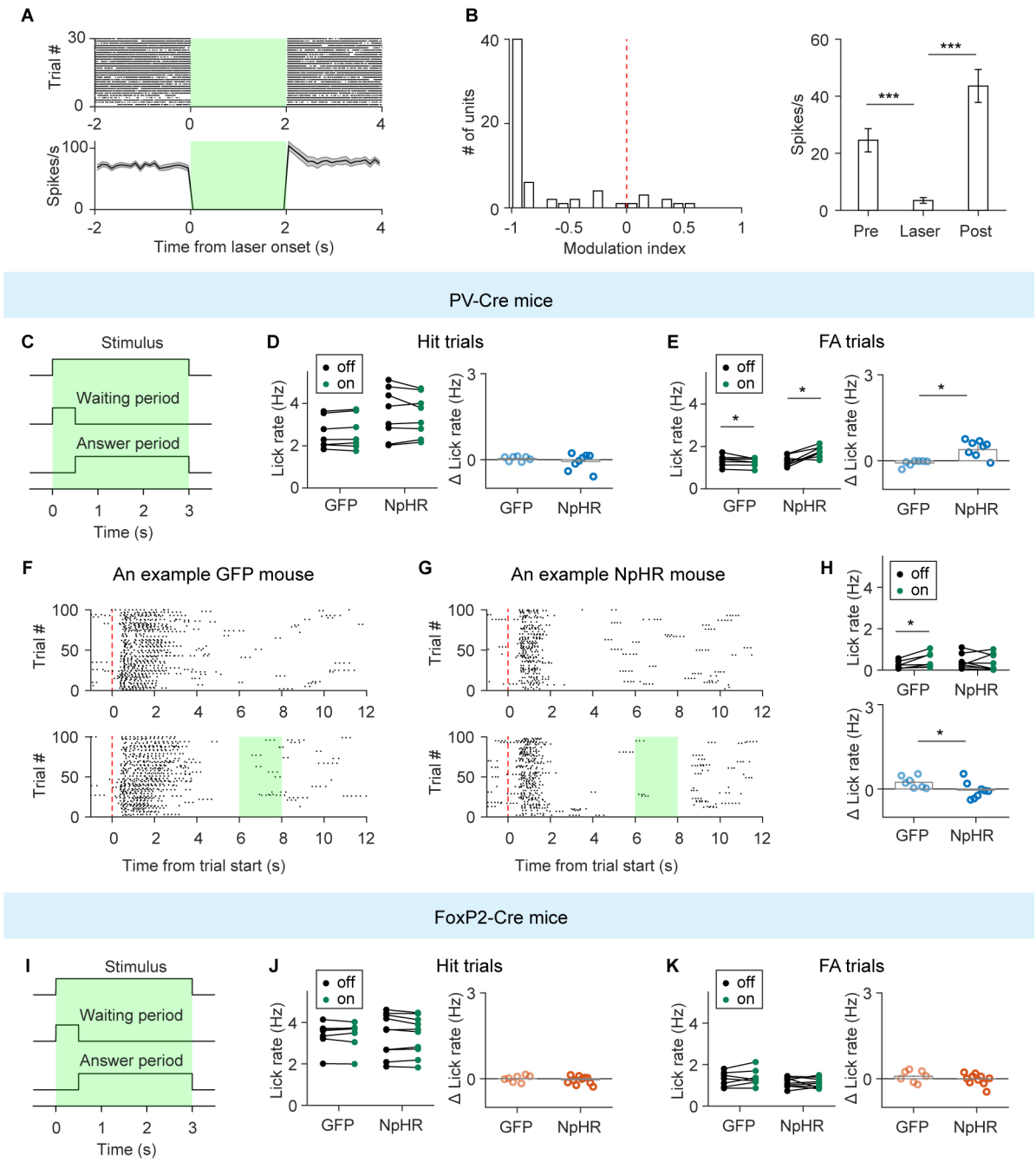

Figure S2. Effect of inactivating PV or FoxP2 GPe neurons on lick rate during stimulus period or ITI. Related to Figure 2.

(A) Spike raster and PSTH of spontaneous firing from an example GPe neuron recorded in an awake PV-Cre mouse expressing AAV-DIO-NpHR in the GPe. Green shading indicates the laser stimulation period.

(B) Optogenetic activation of NpHR significantly suppressed spontaneous firing of GPe neurons in PV-Cre mice expressing AAV-DIO-NpHR in the GPe. Left, distribution of modulation index, defined as $(R_{laser} - R_{pre})/(R_{laser} + R_{pre})$, in which R_{laser} and R_{pre} are the firing rates within a 2-s period during and before laser stimulation, respectively. $p = 6.0\times10^{-11}$, n = 64, Wilcoxon signed rank test. Right, average firing rates before, during, and after laser stimulation. *** $p < 0.001$, one-way repeated measures ANOVA followed by Sidak's multiple comparisons test.

(C) Schematic of the duration of laser stimulation (green shading) during stimulus presentation period.

(D) Left, lick rates during stimulus period in Hit trials under laser-off and laser-on conditions for PV-Cre mice expressing AAV-FLEX-EGFP (n = 7) or AAV-DIO-NpHR (n = 8) in the GPe. Right, comparison of lick rate difference between

GFP and NpHR mice. $p = 0.78$, Wilcoxon rank-sum test.

(E) Same as (C), but for FA trials. $*p < 0.05$. Left, Wilcoxon signed-rank test. Right, Wilcoxon rank-sum test.

(F) Lick rasters from an example PV-Cre mouse expressing AAV-FLEX-EGFP in the GPe. Top, laser-off trials. Bottom, trials with laser stimulation during the ITI. Green shading, laser stimulation period.

(G) Same as (F), but for a PV-Cre mouse expressing AAV-DIO-NpHR in the GPe.

(H) Top, ITI lick rates under laser-off and laser-on conditions for GFP mice ($n = 7$, $p = 0.016$, Wilcoxon signed-rank test) and NpHR PV-Cre mice ($n = 8$, $p = 0.46$, Wilcoxon signed-rank test). Bottom, comparison of ITI laser-induced lick rate changes between GFP and NpHR PV-Cre mice ($p = 0.025$, Wilcoxon rank-sum test).

(I) Schematic of the duration of laser stimulation during stimulus presentation period.

(J) Left, lick rates during stimulus period in Hit trials under laser-off and laser-on conditions for FoxP2-Cre mice expressing AAV-FLEX-EGFP ($n = 7$) or AAV-DIO-NpHR ($n = 10$) in the GPe. Right, comparison of lick rate difference between GFP and NpHR mice. $p = 0.61$, Wilcoxon rank-sum test.

(K) Same as (J), but for FA trials. $p > 0.05$. Left, Wilcoxon signed-rank test. Right, Wilcoxon rank-sum test.

For display purposes, 100 laser-off trials and 100 laser-on trials were shown in the raster plot. Data represent mean ± SEM.

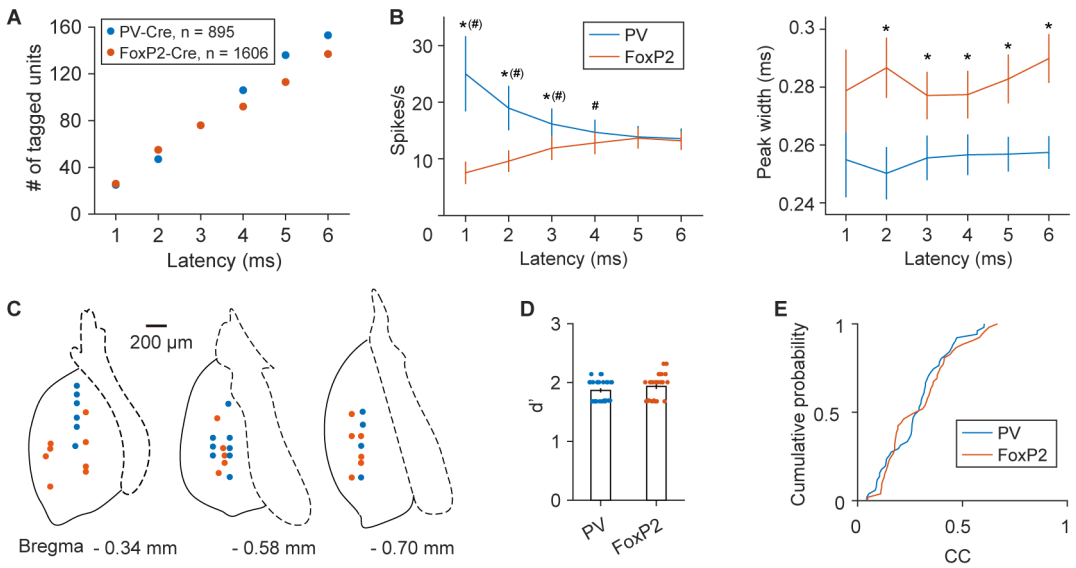

Figure S3. Spatial location and number of identified PV and FoxP2 GPe neurons from behaving mice. Related to Figure 3.

(A) Number of identified PV and FoxP2 GPe neurons across latency thresholds ranging from 1 to 6 ms. A total of 895 neurons were recorded from PV-Cre mice (n = 50 sessions, 8 mice) and 1606 neurons from FoxP2-Cre mice (n = 85 sessions, 14 mice). Only a subset of these were classified as PV or FoxP2 neurons according to the latency criteria.

(B) Left, spontaneous firing rates of PV and FoxP2 neurons identified under different latency thresholds. *$p < 0.05$, Wilcoxon rank-sum test. #$p < 0.05$, two-sample Kolmogorov-Smirnov test. Right, spike waveform peak widths of the same populations. *$p < 0.05$, Wilcoxon rank-sum test.

(C) Recording locations of optogenetically identified PV (blue) and FoxP2 (brown) neurons in the GPe.

(D) Behavioral performance of PV-Cre mice and FoxP2-Cre mice in which PV and FoxP2 neurons were identified using a 3-ms latency threshold. $p = 0.29$, Wilcoxon rank-sum test.

(E) The correlation coefficients (CCs) between GLM-predicted and actual activity were calculated separately for PV and FoxP2 neurons identified using a 3-ms latency threshold. The distributions of CCs did not differ significantly ($p = 0.59$, n = 51 and 52 for PV and FoxP2 neurons, respectively, two-sample Kolmogorov-Smirnov test).

Data represent mean ± SEM.

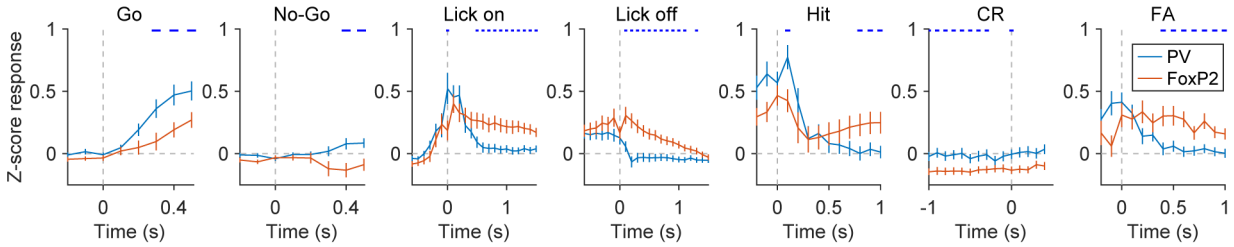

Figure S4. Event-aligned Z-scored responses of task-modulated PV and FoxP2 GPe neurons identified using a 3-ms latency threshold. Related to Figure 5.

Average Z-scored neural activity aligned to stimulus onset (in Go and No-Go trials), lick-bout onset, lick-bout offset, and outcome onset (Hit, CR, and FA). Blue, PV neurons (n = 51). Brown, FoxP2 neurons (n = 52). Horizontal ticks mark time points with significant differences between the two cell types ($p < 0.05$), determined by a two-way ANOVA with mixed design followed by Tukey's multiple comparisons test. For each event type, the two-way ANOVA was applied only to time points within specified time windows: Go or No-Go stimulus, 0 – 0.5 s; lick-bout onset, 0 – 1.5 s; lick-bout offset, 0 – 1.5 s; Hit, 0 – 1 s; CR, -1 – 0 s (with time zero defined as the end of the answer period); and FA, 0 – 1 s. Data represent mean ± SEM.

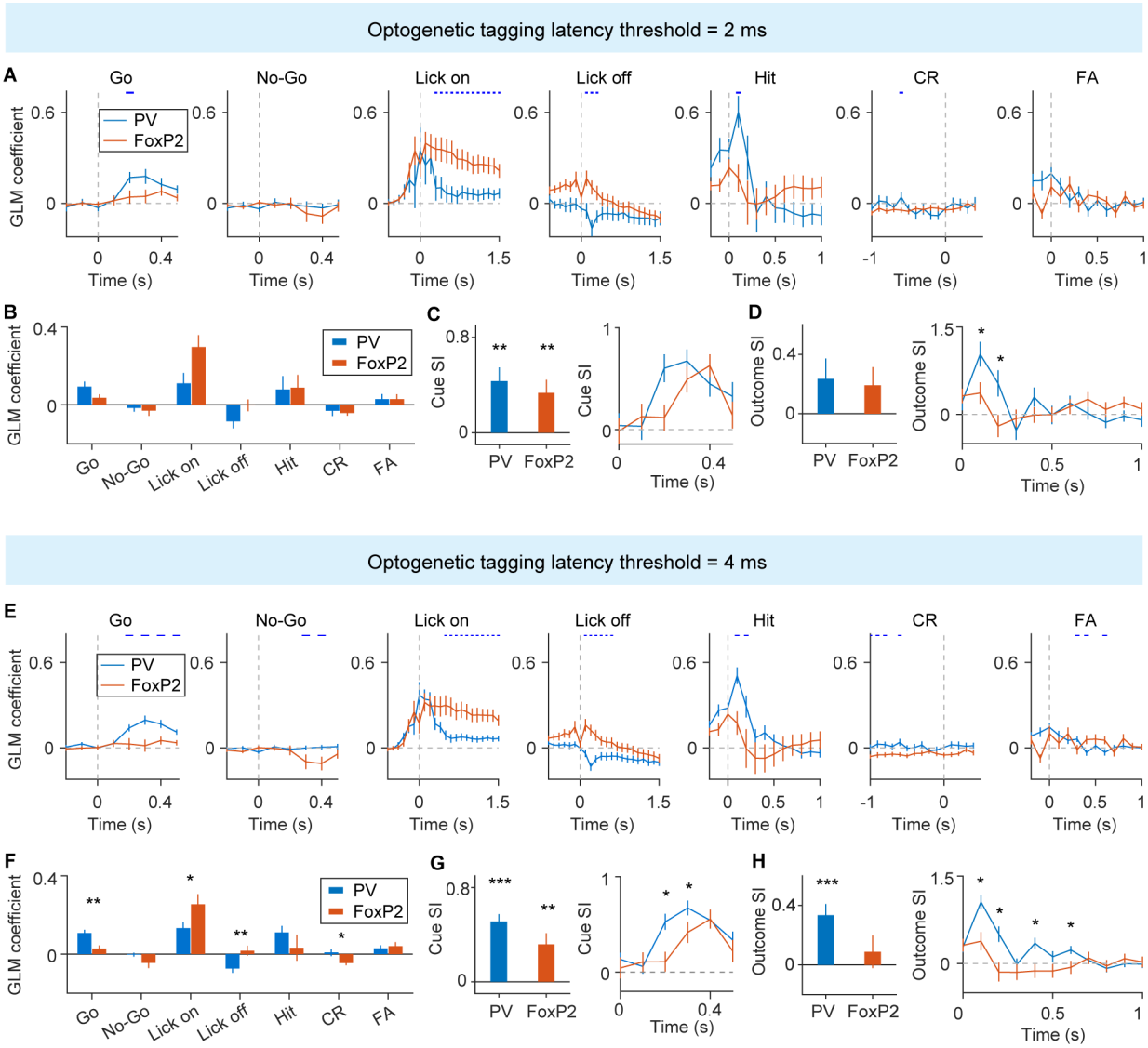

Figure S5. Comparison of GLM coefficients between task-modulated PV and FoxP2 GPe neurons identified using a 2-ms or 4-ms latency threshold. Related to Figure 5.

(A–D) Analyses for PV (n=28) and FoxP2 (n=38) GPe neurons identified with a 2-ms latency threshold:

(A) Temporal profiles of GLM coefficient averaged across PV neurons (n=28) or FoxP2 neurons (n=38) for each regressor. Horizontal ticks indicate time points where GLM coefficients differed significantly between PV and FoxP2 neurons ($p < 0.05$), determined by a two-way ANOVA with mixed design followed by Tukey's multiple comparisons test. For each regressor, the two-way ANOVA was applied only to time points within specified time windows: Go or No-Go stimulus, 0 – 0.5 s; lick-bout onset, 0 – 1.5 s; lick-bout offset, 0 – 1.5 s; Hit, 0 – 1 s; CR, -1 – 0 s (with time zero defined as the end of the answer period); and FA, 0 – 1 s.

(B) Mean GLM coefficients for each regressor, averaged over a defined time window, compared between PV and FoxP2 neurons.

(C) Left, cue SI was significantly larger than 0 for both PV and FoxP2 GPe neurons ($p < 0.01$, Wilcoxon signed-rank test) , with no significant difference between the two cell types ($p = 0.77$, Wilcoxon rank-sum test). Right, temporal dynamics of cue SI in PV versus FoxP2 neurons.

(D) Left, outcome SI of PV neurons and FoxP2 neurons. Right, temporal dynamics of outcome SI in PV versus FoxP2 neurons. * $p < 0.05$, two-way ANOVA with mixed design ($F_{(10, 640)} = 4.10$, $p_{interaction} = 0.0034$) followed by Tukey's multiple comparisons test.

(E–H) Same analyses as (A–D), applied to PV neurons (n = 71) and FoxP2 (n = 52) GPe neurons identified using a 4-ms latency threshold.

(E) Temporal profiles of GLM coefficient averaged across PV neurons (n=71) or FoxP2 neurons (n=52) for each regressor. Horizontal ticks indicate time points where GLM coefficients differed significantly between PV and FoxP2 neurons ($p < 0.05$), determined by a two-way ANOVA with mixed design followed by Tukey's multiple comparisons test.

(F) Mean GLM coefficients for each regressor, averaged over a defined time window, compared between PV and FoxP2 neurons. *$p < 0.05$, **$p < 0.01$, two-way ANOVA with mixed design followed by Tukey's multiple comparisons test.

(G) Left, cue SI was significantly larger than 0 for both PV and FoxP2 GPe neurons ($p <0.01$, Wilcoxon signed-rank test), with no significant difference between the two cell types ($p = 0.26$, Wilcoxon rank-sum test). Right, temporal dynamics of cue SI in PV versus FoxP2 neurons. *$p < 0.05$, two-way ANOVA with mixed design ($F_{(1, 121)} = 4.02$, $p = 0.047$) followed by Tukey's multiple comparisons test.

(H) Left, outcome SI of PV neurons was significantly greater than zero ($p = 9.7\times10^{-5}$, Wilcoxon signed-rank test), whereas that of FoxP2 neurons did not differ significantly from zero ($p = 0.43$, Wilcoxon signed-rank test). Right, temporal dynamics of outcome SI in PV versus FoxP2 neurons. *$p < 0.05$, two-way ANOVA with mixed design ($F_{(1, 121)} = 5.94$, $p = 0.016$) followed by Tukey's multiple comparisons test.

Data represent mean ± SEM.

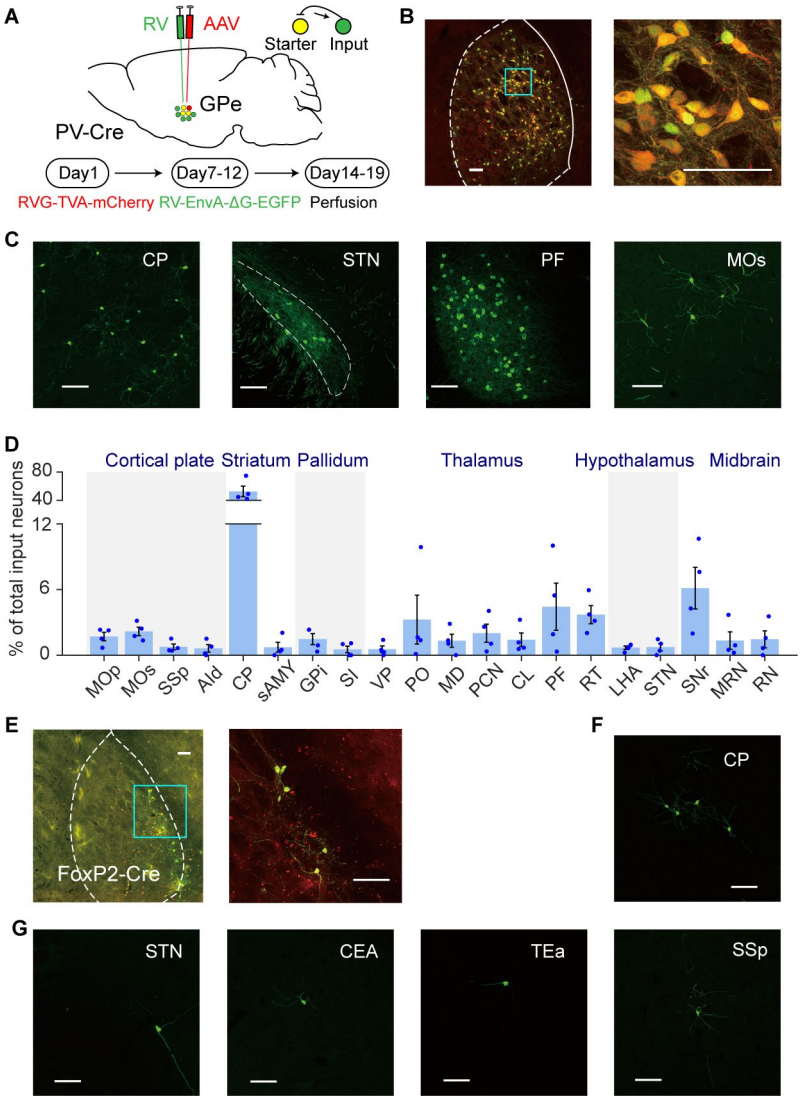

Figure S6. Monosynaptic inputs to PV and FoxP2 GPe neurons. Related to Figure 5.

(A) Virus tracing strategy.

(B) Example fluorescence images showing starter cells (co-expressing mCherry and EGFP) in the GPe of a PV-Cre mouse.

(C) Representative fluorescence images in selected brain regions showing RV-labeled input cells to PV GPe neurons.

(D) Whole-brain distributions of input neurons to PV GPe neurons (n = 4 PV-Cre mice).

(E) Example fluorescence images showing starter cells co-expressing mCherry and EGFP in the GPe of a FoxP2-Cre mouse.

(F) Representative fluorescence images of RV-labeled input neurons in the striatum (caudoputamen, CP) projecting to FoxP2 GPe neurons. Such striatal input neurons were observed in all FoxP2-Cre mice (n=3).

(G) Representative fluorescence images of RV-labeled input neurons projecting to FoxP2 GPe neurons in four additional regions: subthalamic nucleus (STN), central amygdala nucleus (CEA), temporal association areas (TEa), and primary somatosensory area (SSp). Input neurons in these regions were detected in only 1 of 3 FoxP2-Cre mice.

Scale bars, 100 μm.

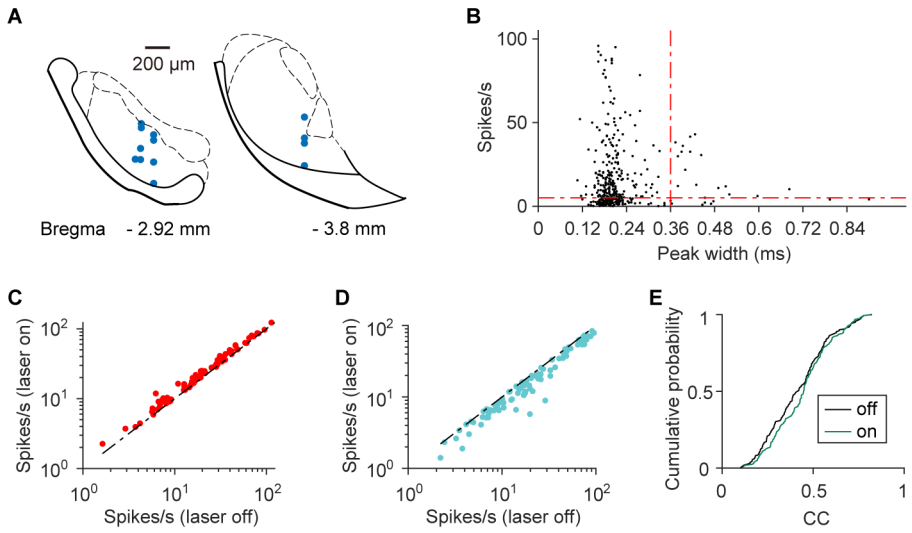

Figure S7. Recording sites, identification of putative GABAergic SNr neurons, firing rate changes, and GLM performance of SNr neurons. Related to Figure 7.

(A) Recording locations of SNr neurons. Each dot represents the position of electrode tip in the last recording session for each mouse. Scale bars, 200 µm.

(B) Putative GABAergic SNr units were identified by a spike peak width < 0.36 ms, and only neurons with baseline firing rates > 5 Hz were included in subsequent analyses.

(C) In a subset of SNr neurons (n = 74), inactivation of GPe PV neurons significantly increased mean firing rates. The mean firing rate of each neuron was calculated from 0–3 s after stimulus onset, and significance was determined by comparing laser-off and laser-on trials (Go or No-Go) using a two-way ANOVA on 100-ms binned PSTHs ($p < 0.01$).

(D) In another subset of SNr neurons (n = 88), inactivation of GPe PV neurons significantly decreased mean firing rates.

(E) For neurons with significant firing rate change, the correlation coefficients (CCs) between GLM-predicted and actual activity were calculated separately for laser-off and laser-on trials. The distributions of CCs under the two conditions did not differ significantly ($p = 0.20$, n = 162, two-sample Kolmogorov-Smirnov test).